ELSEVIER

Topology of flow and heat transfer from prisms in square array

Zhanying Zheng [a], Md. Mahbub Alam [a,*], Qinmin Zheng [b], S. Dhinakaran [c], Md. Islam [d]

[a] Center for Turbulence Control, Harbin Institute of Technology (Shenzhen), Shenzhen 518055, China
[b] Department of Mechanics and Aerospace Engineering, Southern University of Science and Technology, Shenzhen 518055, China
[c] The Centre for Fluid Dynamics, Department of Mechanical Engineering, Indian Institute of Technology Indore, Simrol, Indore 453 552, India
[d] Mechanical Engineering Department, Khalifa University of Science and Technology, Abu Dhabi 2533, United Arab Emirates

ARTICLE INFO

ABSTRACT

Structures in an array with multiple rows and columns may undergo both inline and side-by-side interferences. A system of nine square prisms in a 3×3 square array is numerically investigated for pitch ratio $L/D = 1.2 - 7.0$ at a Reynolds number of 150, where L is the spacing between the centers of two adjacent prisms, and D is the side width of a square prism. The focus is given on investigating the effect of L/D on flow topology, fluid forces, heat transfer, vortex shedding, and recirculation bubbles. An increase in L/D from 1.2 to 7.0 leads to evolutions of five distinct flows: single bluff body flow ($L/D < 1.6$), reattachment flow ($1.6 < L/D < 3.3$), lateral-interaction-induced coshedding flow ($3.3 < L/D < 4.1$), mixed flow ($4.1 < L/D < 4.6$) and free coshedding flow ($4.6 < L/D < 7.0$). The reattachment flow corresponds to small fluid forces while the lateral-interaction-induced coshedding flow induces large fluid forces. The time-mean drag force coefficient of the center prism drastically increases from 0.09 to 1.0 as the flow evolves from the reattachment flow to the lateral-interaction-induced coshedding flow. The maximum heat transfer from the center prism, 10% higher than that from a standalone prism, occurs for the lateral-interaction-induced coshedding flow where the flow around the center prism resembles creeping flow, no recirculation bubble forming on the front or rear surface of the prism. The coherence between heat transfer and flow patterns is discussed, including the impacts of shear layer reattachment, flow recirculation, and vortex shedding on heat transfer.

1. Introduction

Engineering structures generally appear in a group. Fluid dynamics around and heat transfer from the structures are crucial for the design of the structures. Compared with a single isolated structure, closely spaced multiple structures involve many complex flow phenomena, including flow reattachment, shear-layer and vortex impingement, quasi-periodic vortices, gap flow instability, interacting streets and so on. It is, therefore, of fundamental and practical interest to investigate the detailed physics of the relevant flow and heat transfer problems. The simplest configurations of multiple structures are two structures arranged in tandem [1–9], side-by-side [10–12] or staggered [13–16]. During the last decades, many investigations have been conducted on circular cylinders [17,18] whilst the flow and heat transfer around multiple square prisms have received relatively less attention, despite their significance in engineering [19]. Different from a circular cylinder undergoing oscillating flow-separation points, a square prism is characterized by a fixed flow separation point. It is, therefore, expected that the two

representative models (circular- and square-sectioned cylinders) have substantially distinct fluid dynamics from each other.

For flow around two side-by-side square prisms at a Reynolds number $Re = 47,000$, Alam et al. [20] performed a systematic study on the flow field, Strouhal number, and fluid forces on the prisms at spacing ratio $L/D = 1.02 - 6.0$, where L is the center-to-center spacing between the prisms, D is the prism width, and Re is based on the freestream velocity U_∞ and D. Four distinct flow regimes were observed as the prism distance gradually increased: single-body regime ($L/D < 1.3$), two-frequency regime ($1.3 < L/D < 2.2$), transition regime ($2.2 < L/D < 3.0$), and coupled vortex street regime ($3.0 < L/D < 6$). The above flow regimes were classified based on the appearance of various typical flow patterns, such as shear-layer interaction, gap-flow deflection and changeover, flow entrainment, recirculation bubble, and vortex interaction. Compared to Alam et al.'s [20] results at $Re = 47,000$, qualitatively similar observations were also made in flow visualization experiments at a small $Re = 300$ [21]. KolÁŘ et al. [22] studied the turbulent characteristics in the near wake of two side-by-side prisms at $L/D = 3$. A two-component laser Doppler velocimeter was used to

---

Nomenclature

C_D	drag coefficient
$\overline{C_D}$	time-averaged drag coefficient
C_D'	fluctuating drag coefficient
C_L	lift coefficient
C_L'	fluctuating lift coefficient
C_P	pressure coefficient
D	width of the prism
F_x	drag force on prism
F_y	lift force on prism
f_s	vortex shedding frequency
h	heat transfer coefficient
L	centre-to-centre distance between prisms
L_f	vortex formation length
L_{rf}	recirculation bubble size
Nu	nusselt number
p	pressure
p_∞	freestream pressure
Pr	Prandtl number
Re	Reynolds number
St	Strouhal number
t	time
T	temperature
T_∞	freestream temperature
$\boldsymbol{u}$	velocity vector
$\overline{u}$	time-averaged streamwise velocity
u_{rms}	root-mean-square of the streamwise velocity fluctuation
U_∞	freestream velocity
w	prism wake width

Greek symbols

μ	dynamic viscosity
ρ	density

---

measure the flow field. They found formation of coupled vortex street flow at this spacing. Agrawal et al. [12] investigated a low Re ($= 73$) flow around two side-by-side prisms at $L/D = 2.5$ and 0.7, which corresponded to a flip-flop and a synchronised flow, respectively. The difference between the two flows was interpreted in terms of the interaction of the gap flow with the adjoining wakes. Several studies on more than two prisms in side-by-side arrangements are available in the literature. Kumar et al. [23] at $Re = 80$ studied flow around a row of nine square prisms placed normal to the oncoming flow and discussed the effect of L/D ($= 1.3 - 13$) on the flow. Based on the vorticity field and drag coefficient results, three flow regimes were reported with increasing L/D: synchronised, quasi-periodic, and chaotic flows. Sewatkar et al. [24] at $Re = 30$–140 examined the combined effects of L/D and Re on the flow across a row of nine square prisms. The critical Re for the onset of vortex shedding increased with an increase in L/D, and the interaction between the wakes behind the cylinders weakened with increasing Re. Chatterjee et al. [25,26]. studied the hydrodynamics around a row of five square prisms at $Re = 150$. Depending on L/D, three flow patterns were identified: flip-flop pattern, inphase and antiphase synchronized pattern, and non-synchronized pattern. The drag coefficient, lift coefficient, Nusselt number, and Strouhal number were estimated. Zheng and Alam [27] investigated the flow around three side-by-side square prisms at $Re = 150$ and found five distinct flow structures as L/D is varied from 1.1 to 9.0: base-bleed flow ($L/D < 1.4$), flip-flopping flow ($1.4 < L/D < 2.1$), symmetrically biased beat flow ($2.1 < L/D < 2.6$), non-biased beat flow ($2.6 < L/D < 7.25$) and weak interaction flow ($7.25 < L/D < 9.0$). The intrinsic features of the flow and origin of the secondary frequency were systematically elaborated. In addition, vortex formation length and wake width were linked to fluid forces and flow regimes [28].

Studies concerning the flow around multiple tandem square prisms largely involve the simplest case of two tandem prisms. Sakamoto et al. [29] performed measurements of fluctuating forces acting on two tandem prisms at $L/D = 1.5 - 40$. Three flow regimes were identified based on the variation in Strouhal number. Sakamoto and Haniu [30] further studied the effect of freestream turbulence intensity on the fluid forces. Alam et al. [31] studied the flow around two tandem prisms and controlled the forces on the prisms using a flat plate. The maximum reductions in fluctuating lift and drag are 94% and 71% for the upstream prism and 80% and 65% for the downstream prism, respectively. Liu and Chen [32] discussed the flow hysteresis observed around the critical L/D of two square prisms in tandem and examined the hysteresis and Re effects on drag forces, pressure, and Strouhal numbers. Kim et al. [33] measured the flow around two square prisms in a tandem arrangement

using particle image velocimetry and found that the sudden change in the flow pattern arises because of no gap shear layer reattachment on the downstream prism for spacing beyond the critical. Yen et al. [34] used particle image velocimetry to conduct similar measurements, and the flow field was classified into three modes: vortex sheet of the single mode, reattached mode, and binary mode. A numerical investigation conducted by Sohankar [35] confirmed the existence of the above three modes. Rastan and Alam [36] examined the effect of Re and L/D on the flow transitions and flow regimes for both tandem circular and square cylinders. They found that, a higher Re is required to initiate the vortex shedding for two tandem cylinders, compared to the single cylinder counterpart. Freidooni et al. [37] numerically studied the gap and wake flows associated with two inline buildings at $Re = 220,000$ and indicated that wind condition is strong at small gaps, hence a minimum gap-to-length ratio of 3 was recommended. Investigations on the flow for more than two prisms are yet scarce in the literature. Bao et al. [38] studied the flow around a row of six square prisms in tandem at $Re = 100$ and identified six different flow patterns depending on L/D. Sewatkar et al. [39] further studied the chaotic nature of the flow and confirmed the flow regimes using particle image velocimetry. Zheng and Alam [40] systematically studied the evolution of the wake of three inline square prisms and revealed the detailed physics of the evolution of the primary vortex street to the secondary.

Although not as frequent as the side-by-side or tandem arrangement, other cylinder configurations have also been examined in the past. Islam et al. [41] numerically investigated the laminar flow around four rectangular cylinders in the rectangular arrangement and showed the dependence of flow patterns on spacing ratio. Zhang et al. [42] and Abbasi et al. [43] used finite volume and lattice Boltzmann methods, respectively, to study the flow past four square cylinders in an in-line square configuration and observed the changes of the wake patterns. Chatterjee and Biswas [44] carried out simulations of flow around two rows of square cylinders arranged in a staggered fashion and observed the chaotic behavior of the flow for relatively small transverse spacing of the cylinders. Nguyen et al. [45] investigated characteristics of flow around four cylinders of various shapes in a square configuration. They found that the flow around the square cylinders was unstable and the vortices shed from the rear cylinders merge to the large-scale vortices shed from the freestream sides. The same happened for triangular and hexagons cylinders.

Heat transfer from square prisms is strongly correlated with the surrounding flow characteristics. Chatterjee [46] studied numerically the heat transfer around two isothermal square cylinders arranged in a tandem configuration at low Reynolds numbers ($1 \leq Re \leq 30$). The drag

Table 1
Summary of recent studies on flow and heat transfer around multiple square prisms.

| Refs.	Number of prisms	Prism arrangement	Space ratio (L/D)	Heat transfer included	Reynolds number	Key findings
Alam et al. [20]	Two	Side-by-side	1.02 – 6.0	No	47,000	Four distinct flow regimes were observed as L/D gradually increases.
Alam and Zhou [21]	Two	Side-by-side	1.0 – 5.0	No	300	Flow regimes similar to Alam et al. [20] were observed, and the switch of the gap flow occurred at two different time scales.
KolÁŘ [22]	Two	Side-by-side	3.0	No	23,100	The formation of coupled vortex street flow was found at $L/D = 3.0$.
Agrawal et al. [12]	Two	Side-by-side	1.7, 3.5	No	73	The difference between the synchronised and flip-flop flows was attributed to the interaction of the gap flow with the adjoining wakes.
Kumar et al. [23]	Nine	Side-by-side	1.3 – 13	No	80	Three flow regimes were reported, depending on L/D: synchronised, quasi-periodic, and chaotic flows.
Sewatkar et al. [24]	Nine	Side-by-side	1.0 – 4.0	No	30 – 140	The critical Re for the onset of vortex shedding increased with increasing L/D, and the interaction between the wakes behind the cylinders was weakened with increasing Re.
Chatterjee et al. [25,26].	Five	Side-by-side	1.2 – 4.0	Yes	150	Depending on L/D, three flow patterns were identified: flip-flop pattern, inphase and antiphase synchronized pattern, and non-synchronized pattern.
Zheng and Alam [27]	Three	Side-by-side	1.1 – 9.0	No	150	Five distinct flow structures were found as L/D is varied from 1.1 to 9.0.
Sakamoto et al. [29]	Two	Tandem	1.5 – 40	No	55,200	Three flow regimes were identified based on the variation in Strouhal number.
Sakamoto and Haniu [30]	Two	Tandem	1.0 – 7.0	No	33,200	The effect of freestream turbulence intensity on the fluid forces was studied, and the addition of turbulent intensity caused the Strouhal number to decrease or increase, depending on the flow regimes.
Alam et al. [31]	Two	Tandem	1.0 – 11.0	No	56,000	The fluid forces were controlled using a flat plate, and maximum reductions in fluctuation drag and lift were 94% and 71% for the upstream prism and 80% and 65% for the downstream prism, respectively.
Liu and Chen [32]	Two	Tandem	1.5 – 9.0	No	2000 – 16,000	The flow hysteresis and Re effect were studied.
Kim et al. [33]	Two	Tandem	1.5 – 11.0	No	5300, 16,000	The abrupt change of flow patterns at the critical L/D was studied.
Yen et al. [34]	Two	Tandem	1.0 – 6.0	No	300 – 1000	The flow field was classified into three modes depending on Re and L/D: single mode, reattached mode, and binary mode.
Sohankar [35]	Two	Tandem	1.3 – 13	No	40 – 1000	Three major flow regimes were distinguished depending on L/D: single slender-body regime, reattachment regime, coshedding or binary vortex regime. The hysteresis limit was sensitive to Re.
Rastan and Alam [36]	Two	Tandem	1.0 – 7.0	No	< 20,000	A higher Re was required to initiate the vortex shedding from two tandem prisms, compared to the single prism counterpart.
Freidooni et al. [37]	Two	Tandem	2.0 – 6.0	No	220,000	Wind was strong at small L/D, and hence a minimum $L/D = 3$ was recommended.
Bao et al. [38]	Six	Tandem	1.5 – 15	No	100	Six different flow patterns were identified, depending on L/D.
Sewatkar et al. [39]	Six	Tandem	2.5 – 12	No	80 – 320	Four flow regimes were observed. The numerical simulations was confirmed via particle-image-velocimetry experiments.
Zheng & Alam [40]	Three	Tandem	1.2 – 10.0	No	150	Evolution of the wake of three inline square prisms was systematically studied, and the detailed physics of the evolution of the primary vortex street to the secondary was revealed.
Islam et al. [41]	Four	Rectangular	1.5 – 11	No	100	Effects of L/D on various physical quantities were studied, and the mean drag coefficient of the downstream prism was smaller than that of the single prism.
Abbasi et al. [43]	Four	In-line square	2, 4, 7	No	60 – 175	Four distinct wake patterns were observed: steady wake pattern, stable shielding wake pattern, wiggling shielding wake pattern, and vortex shedding wake pattern.
Chatterjee & Biswas [44]	Two rows	Staggered	2 – 6	No	100	Chaotic behavior of the flow was observed at relatively small transverse spacing of the cylinders
Nguyen et al. [45]	Four	Square	3	No	65 – 300	Flow was unstable, and vortices shed from the gap merge with the large-scale vortices shed from the freestream sides.
Chatterjee [46]	Two	Tandem	5	Yes	1 – 30	Drag coefficient decreased and Nusselt number increased with Re, and the front surfaces of the cylinders experienced more heat transfer than the other surfaces.
Chatterjee [47]	Two	Tandem	2 – 11	Yes	50 – 150	Nusselt number increased with L/D for both cylinders, and the average Nusselt number of the upstream cylinder approached that of a single cylinder when L/D was increased.
Huang et al. [49]	Two	Tandem	5	Yes	80 – 150	The flow was time-periodic unsteady whilst the total heat transfer from both cylinders enhanced with increasing Re.
Sanyal & Dhiman [53, 54]	Two	Side-by-side	1.7 – 11	Yes	1 – 40	Several flow regimes depending on L/D were identified, and heat transfer effect on the flow development was determined.
Patel et al. [55]	Two	Side-by-side	3	Yes	100	Nusselt number was higher for the left cylinder when the prisms were rotated in the clockwise direction.
Moussaoui et al. [56]	Three	Vee-shaped	2, 3	Yes	10 – 100	Effect of L/D on local Nusselt number profiles for each block was discussed in detail.
Teixeira et al. [58]	Three	Triangular	2.0 – 5.0	Yes	22,000	Prism arrangement had a strong influence over performance and transient patterns of turbulent flows.
Present	Nine	Square	1.2 – 7.0	Yes	150	–
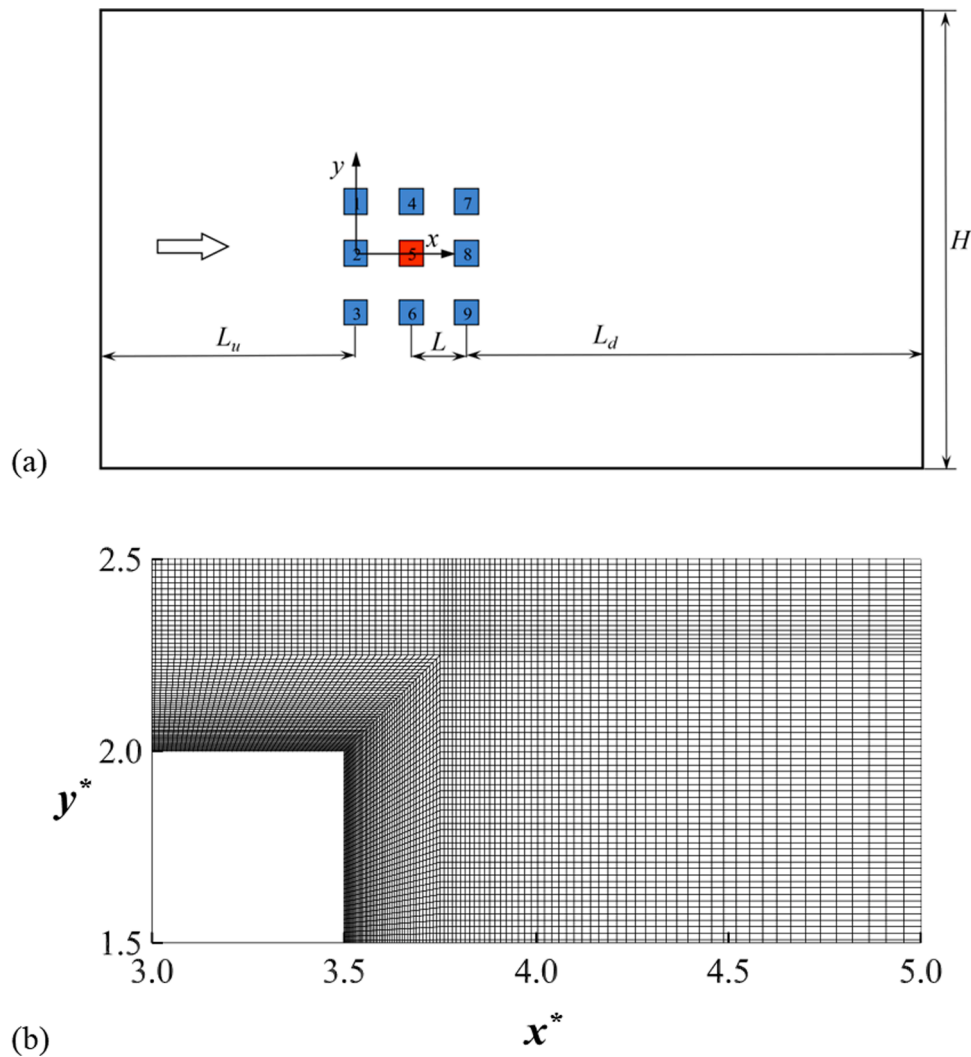
Fig. 1. (a) Computational domain and arrangement of nine prisms in 3 × 3 configurations. The computational domain consists of an inlet (left side), an outlet (right side), and two symmetric (upper and lower sides) boundaries. The flow inlet and outlet are set to be $L_u = 45D$ and $L_d = 90D$, respectively. The height of the computational domain is $H = 85D$. (b) Grid distributions in the vicinity of prism surfaces. A structured grid system is used, and the grid is refined around the prisms.

Table 2
Results for single prism with different grid numbers.

Mesh	$\overline{C}_D$	C'_D	C'_L	St
$N = 60,000$; $\Delta t^* = 0.1558$	1.5012	0.0174	0.2992	0.1544
$N = 121,000$; $\Delta t^* = 0.0779$	1.4832	0.0167	0.2773	0.1579
$N = 200,000$; $\Delta t^* = 0.0390$	1.4790	0.0159	0.2799	0.1584

Table 3
Comparison of simulated force coefficients and Strouhal Number of a single prism with literature data at $Re = 150$.

Parameter	$\overline{C}_D$	C'_D	C'_L	St
Present	1.4832	0.0167	0.2773	0.1579
Sharma and Eswaran [65]	1.4667	–	–	0.1588
Saha et al. [66]	–	0.0170	0.2740	–
Kumar et al. [23]	1.5296	–	–	0.1579
Zafar and Alam [62]	1.4920	0.0155	0.2710	0.1549
Abdelhamid et al. [64]	1.4920	0.0155	0.271	0.1549

Table 4
Simulated time-averaged Nusselt Numbers for different surfaces (Nu_{front}, Nu_{side}, Nu_{rear}) and the whole prism (Nu) at $Re = 150$.

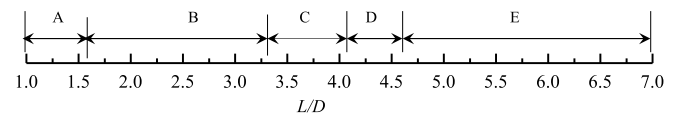| Parameter	Nu_{front}	Nu_{side}	Nu_{rear}	Nu
Present	9.1938	3.7823	2.6782	4.8591
Sharma and Eswaran [65]	9.1202	3.7954	2.5227	4.8343
Sahu et al. [67]	8.9700	3.7500	2.6200	4.8531

Fig. 2. Flow classification and dependence on L/D for the 3 × 3 prism array arrangement according to the evolution of flow structure: A, single bluff body flow ($L/D < 1.6$); B, reattachment flow ($1.6 < L/D < 3.3$); C, lateral-interaction-induced coshedding flow ($3.3 < L/D < 4.1$); D, mixed (reattachment + coshedding) flow ($4.1 < L/D < 4.6$); E, free coshedding flow ($4.6 < L/D < 7.0$).

coefficient decreased and Nusselt number increased with Re, and the front surfaces of the cylinders experienced more heat transfer than the other surfaces, whilst the downstream cylinder always had a higher heat

transfer compared with the upstream one. The Nusselt number increased with L/D for both cylinders, and the average Nusselt number of the upstream cylinder approached that of a single cylinder when L/D was
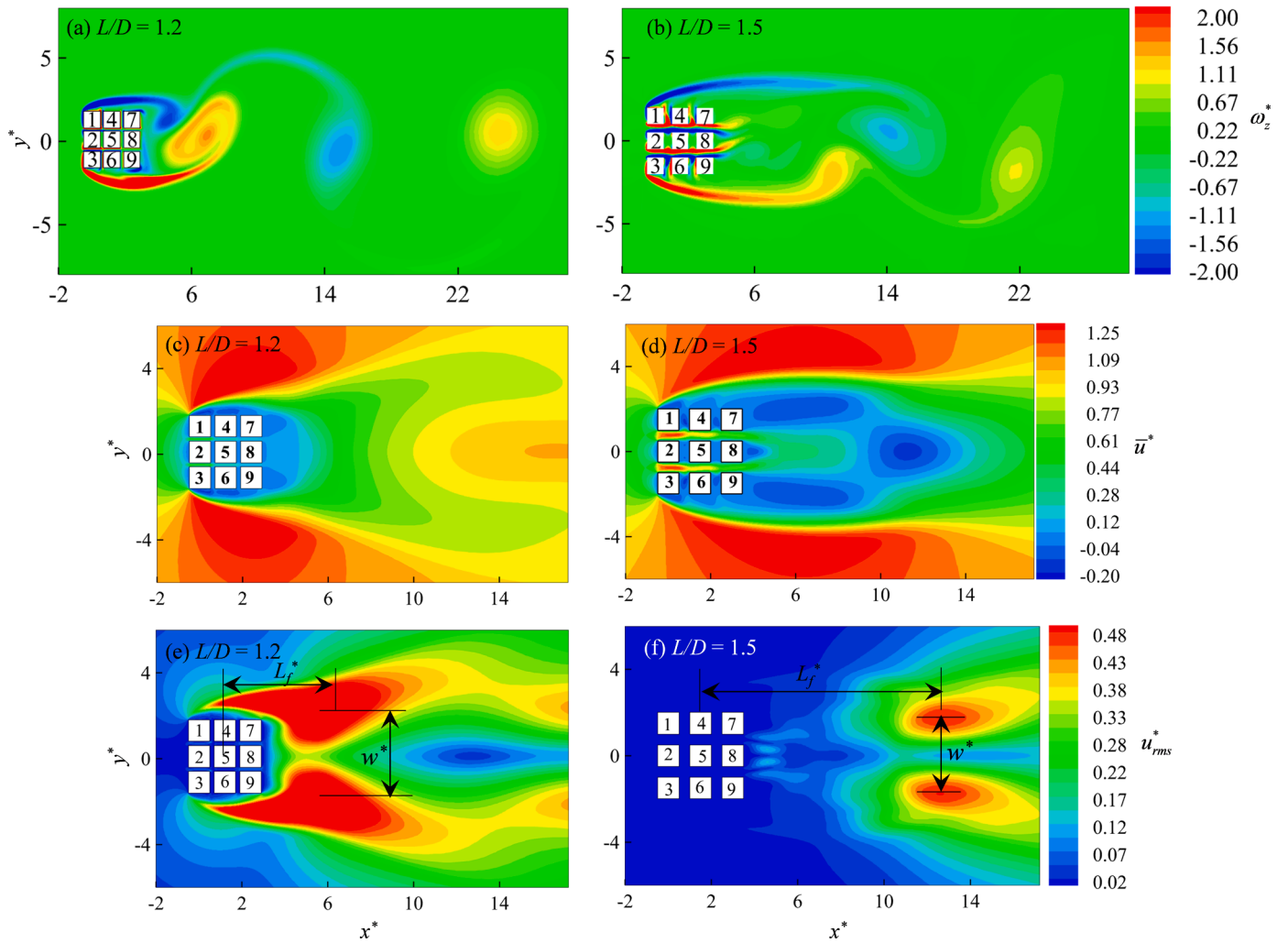
Fig. 3. (a, b) Contours of instantaneous vorticity, showing alternating vortex shedding from the freestream sides. All nine prisms act as a single square block whist the gap flows between the three rows of prisms are weak. (c, d) Contours of time-averaged streamwise velocity $\bar{u}^*$, indicating the gap flows are either negligible (c) or diminished rapidly along the flow direction (d). (e, f) Contours of fluctuating velocity u_{rms}^*, where the vortex formation length L_f^* ($= L_f/D$) and wake width w^* ($= w/D$) are marked. (a, c, e) $L/D = 1.2$; (b, d, f) $L/D = 1.5$. Regime A: single bluff body flow.

increased [47]. Chatterjee and Mondal [48] further studied the heat transfer from tandem square cylinders and found that the heat transfer increases continuously with increasing Re and the upstream cylinder in general has a better heat transfer performance compared with the downstream one. Huang et al. [49] confirmed that the flow over tandem square cylinders is time-periodic unsteady at $80 \leq Re \leq 150$ whilst the total heat transfer from both cylinders enhances when Re is increased.

Sisodia et al. [50] reported the flow and convective heat transfer characteristics past a semi-circular cylinder at incidence with a tandem downstream square cylinder. The Nusselt number increased with the increase of Re for both semi-circular and square cylinders. Dwivedi and Dhiman [51] studied the flow around and heat transfer from tandem cylinders and identified the existence of a critical L/D corresponding to a drastic change in the physical parameters. The Nusselt number of the downstream cylinder is found to be always less than the upstream cylinder. Zhang et al. [52] investigated the heat transfer from tandem cylinders with rounded corners. The unsteady near-wake flow behind the downstream cylinder was accompanied by drastic variations of thermal quantities. Apart from the tandem arrangement, Sanyal and Dhiman [53] studied the heat transfer from a pair of side-by-side square cylinders and identified several flow regimes depending on L/D. The heat transfer and its effect on the flow development were determined numerically. The effect of thermal buoyancy on the flow field was

studied in [54]. Patel et al. [55] numerically investigated the heat transfer from side-by-side square cylinders at different angles of incidence. The Nusselt number was higher for the left cylinder when the cylinders are rotated in the clockwise direction. Moussaoui et al. [56] solved the flow and temperature fields around three heated square cylinders arranged in a vee-shaped configuration using the lattice Boltzmann model. They focused on the effect of spacing on local Nusselt number profiles for each block. Barros et al. [57] numerically examined triangular arrangements of cylinders and optimized the cylinder arrangement to obtain maximum Nusselt number. Teixeira et al. [58] also made a similar investigation.

The above studies are summarized in Table 1, with key information of each study listed for comparison, including the number and arrangement of prims, range of L/D, Reynolds number, and whether heat transfer was included not. Hitherto, most studies have focused on prisms arranged either side-by-side or tandem. A few studies adopted more complex scenarios, such as a row of nine prisms or a square arrangement of four prisms. In many engineering applications, a prism is surrounded by both inline and side-by-side neighboring prisms, and a good example is pin fins used for the cooling of microchips. Relevant flow and heat transfer behaviors cannot be simply predicted from the results of two prisms or even two-row arrangements. Considering an arbitrary prism within an array, its flow and heat transfer are potentially
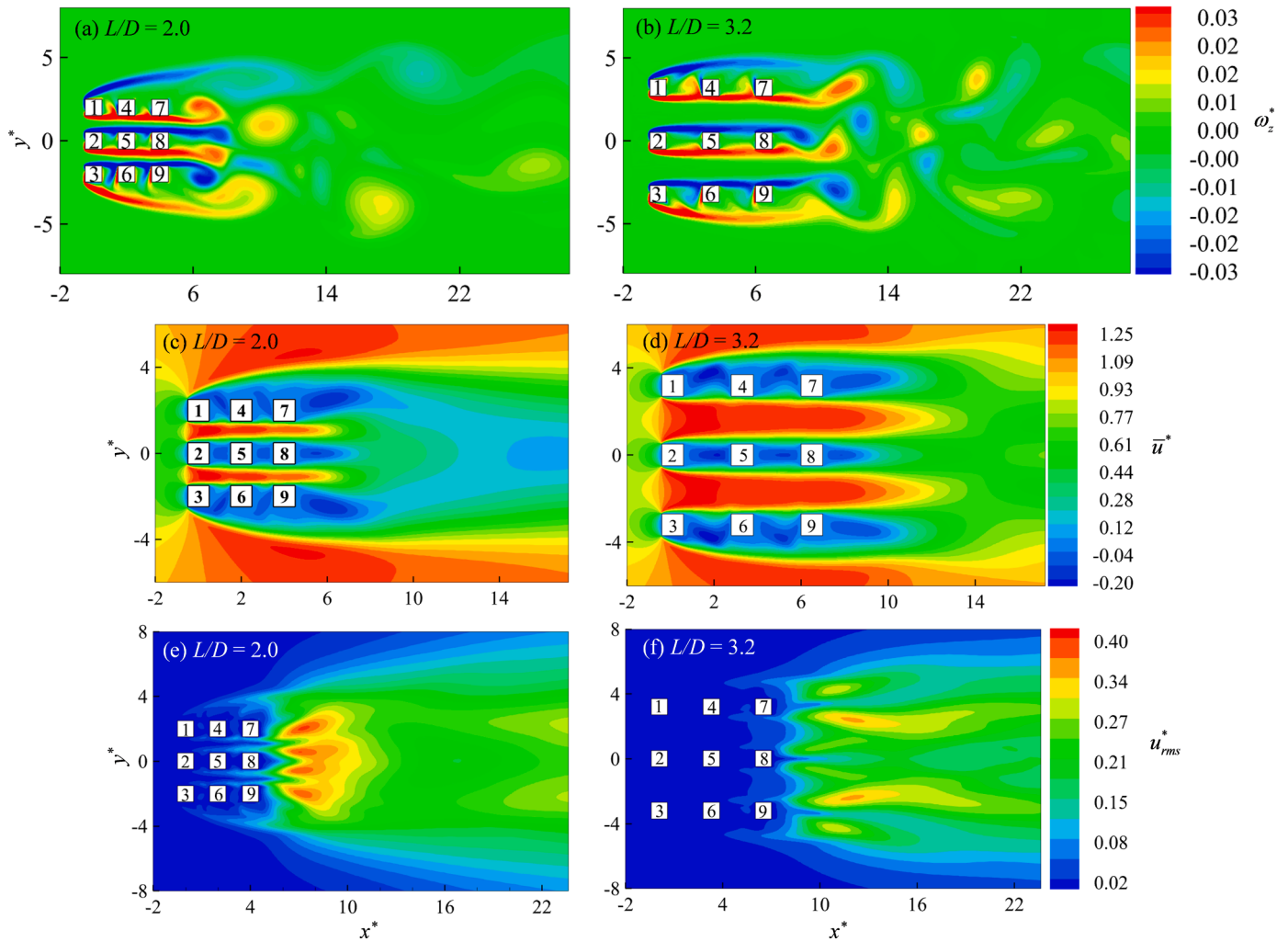
Fig. 4. (a, b) Contours of instantaneous vorticity, showing three vortex streets immediately behind the block, which then evolve into a single street further downstream. The flow becomes chaotic due to a strong interaction between the three streets. (c, d) Contours of time-averaged streamwise velocity $\bar{u}^*$, showing that the gap flows are pronounced to generate three vortex streets. (e, f) Contours of fluctuating velocity u_{rms}^*, indicating the weakened vortex shedding. (a, c, e) $L/D = 2.0$; (b, d, f) $L/D = 3.2$. Regime B: reattachment flow.

affected by all neighboring structures, and hence a 3 × 3 prism array is a minimum requirement for capturing the combined effect of lateral and streamwise interactions. This configuration has not been studied in the past. The objective of this study is to systematically examine the flow and heat transfer of the above configuration and gain a comprehensive understanding of the evolvement of flow regimes and the combined effect of both streamwise and lateral interactions within the prism array so that a more realistic prediction of the flow and heat transfer in practical applications can be realized.

2. Methodologies

Computational methodologies used in this study are described in this section, including the flow and heat transfer governing equations, details of the computational domain and grids, as well as the validation of the numerical model.

2.1. Governing equations

The two-dimensional incompressible Navier-Stokes equations in dimensionless forms can be expressed as follows.

$$\nabla \cdot \mathbf{u}^* = 0, \tag{1}$$

$$\frac{\partial \mathbf{u}^*}{\partial t^*} + (\mathbf{u}^* \nabla)\mathbf{u}^* = -\nabla p^* + \frac{1}{Re}\nabla^2 \mathbf{u}^*, \text{ and} \tag{2}$$

$$\frac{\partial T^*}{\partial t^*} + T^* \nabla T^* = \frac{1}{RePr}\nabla^2 T^*, \tag{3}$$

where all quantities are normalised by the freestream velocity U_∞, the freestream temperature T_∞, and the prism width D. The non-dimensional velocity vector, fluid pressure, time, and temperature are denoted by $\mathbf{u}^*$, p^*, t^* and T^*, respectively, while Re and Pr are the Reynolds number and Prandtl number, respectively. The Reynolds number in this study is defined as

$$Re = \frac{\rho U_\infty D}{\mu} \tag{4}$$

where ρ and μ are the density and dynamic viscosity of the fluid. The Strouhal number St, is defined as

$$St = \frac{f_s D}{U_\infty}, \tag{5}$$

where f_s is the vortex shedding frequency. The drag coefficient C_D, lift coefficient C_L, and pressure coefficient C_p, are, respectively defined as
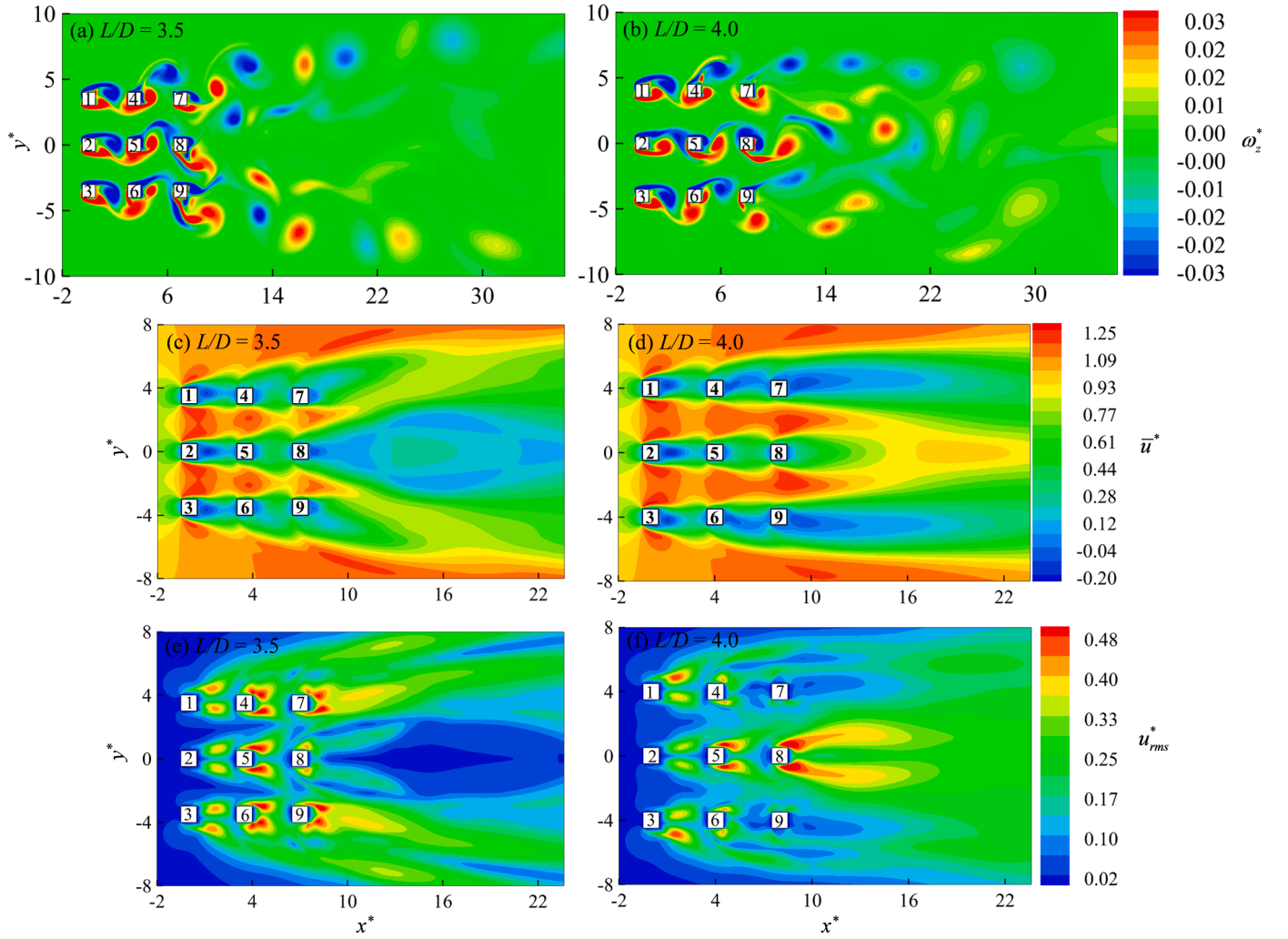
Fig. 5. (a, b) Contours of instantaneous vorticity, showing vortex shedding from individual prisms. Coshedding flow appears at a relatively small L/D compared to a single row of three tandem prisms because of the lateral interaction between different rows of prisms. (c, d) Contours of time–averaged streamwise velocity $\overline{u}^*$, showing a recirculation bubble behind each prism as well as the acceleration of the gap flows as the flow passages contract. (e, f) Contours of fluctuating velocity u_{rms}^*, showing the enhanced vortex shedding from the outer rows (e) or the middle row (f) prisms. (a, c, e) $L/D = 3.5$; (b, d, f) $L/D = 4.0$. Regime C: lateral-interaction-induced coshedding flow.

$$C_D = \frac{2F_x}{\rho D U_\infty^2}, \tag{6}$$

$$C_L = \frac{2F_y}{\rho D U_\infty^2}, \text{ and} \tag{7}$$

$$C_p = \frac{2(p - p_\infty)}{\rho U_\infty^2}, \tag{8}$$

where F_x and F_y are the drag and lift forces, respectively, on a prism. The p and p_∞ are the static pressure at a point on the surface and at the freestream, respectively.

The heat transfer performance of the prism is evaluated using the Nusselt number. The local Nusselt number at point e, surface-averaged Nusselt number, time-averaged Nusselt number and overall Nusselt number (surface- and time-averaged) are, respectively defined as:

$$Nu_e = \frac{h_e D}{k}, \tag{9}$$

$$\langle Nu \rangle = \frac{1}{s} \int_0^s Nu_e ds, \tag{10}$$

$$\overline{Nu} = \frac{1}{T} \int_0^T Nu_e dt, \text{ and} \tag{11}$$

$$Nu = \frac{1}{T} \int_0^T \langle Nu \rangle dt. \tag{12}$$

A commercial code, ANSYS Fluent, has been used to solve the unsteady two-dimensional incompressible Navier-Stokes equations. The PISO algorithm is applied for the pressure-velocity coupling. A second-order upwind differencing scheme is used for the discretization of the convection terms while a second-order implicit forward scheme is adopted for the time marching. The Reynolds number is kept constant at 150. It is known that the onset of vortex shedding from a single prism occurs at $Re \approx 48$ [59], and the flow three-dimensional instability appears at $Re > 200$ [60]. The selection of $Re = 150$ in this study is based on our previous studies on three side-by-side prisms [27] and three tandem prisms [40], which would not only ensure a clear picture of the wake, including shear-layer development, vortex formation, interaction, etc., but also avoid the complexity of the three-dimensional flow (e.g. Kumar et al. [23], $Re = 80$; Sewatkar et al. [24], $30 < Re < 140$; Zheng and Alam [40,61], $Re = 150$). Although a high Re is commonly found in many engineering applications where the flow is three-dimensional, the
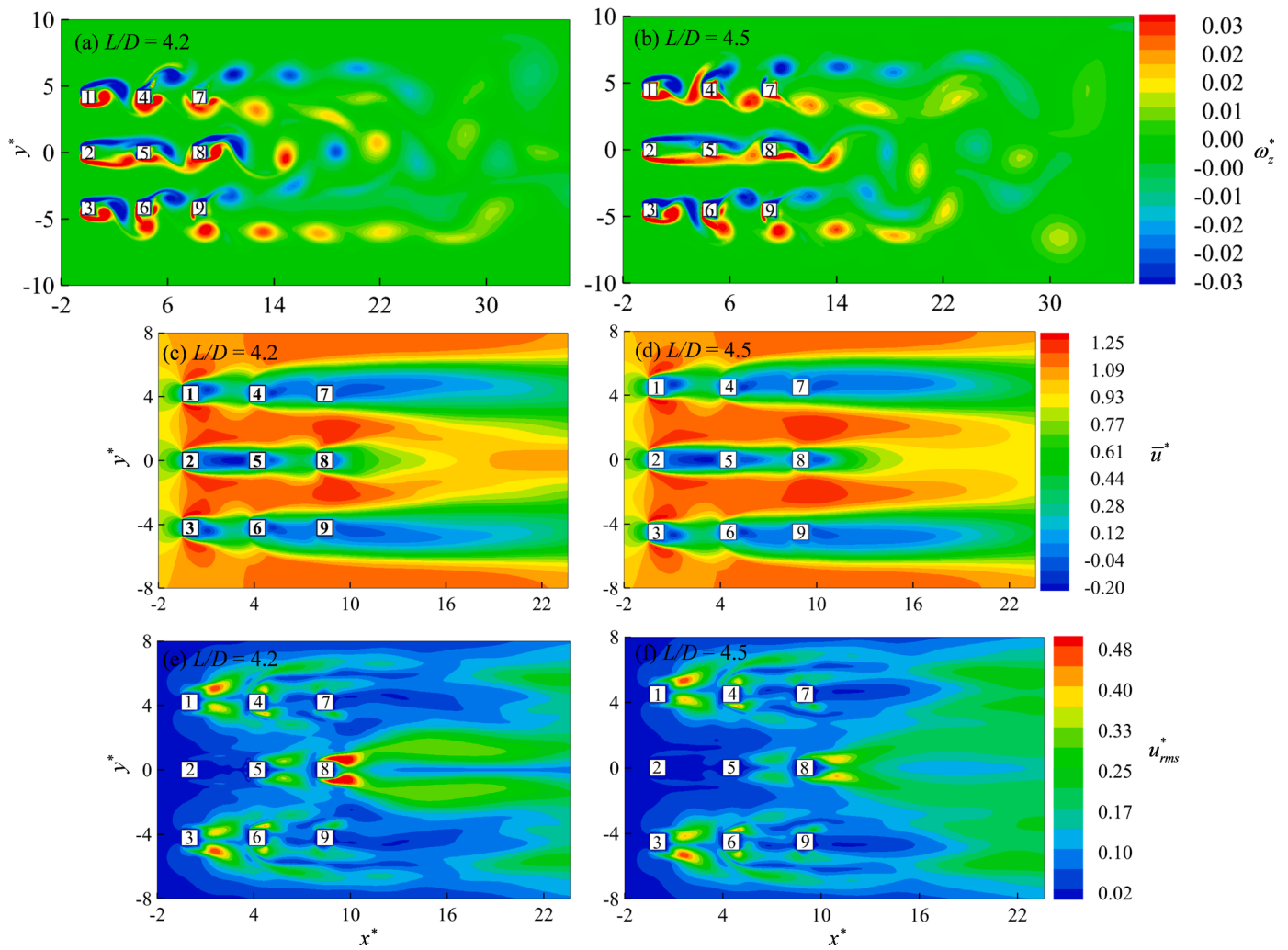
Fig. 6. (a, b) Contours of instantaneous vorticity, showing reattachment flow for the first two prisms of the middle row and coshedding flow for the other prims. (c, d) Contours of time–averaged streamwise velocity $\bar{u}^*$, showing the recirculation bubble behind prism 2 extending up to the front surface of prism 5. (e, f) Contours of fluctuating velocity u^*_{rms}, indicating the vortex shedding is more apparent behind prisms 1, 3 and 8 because of a moderate lateral interaction between different rows of prisms. (a, c, e) $L/D = 4.2$; (b, d, f) $L/D = 4.5$. Regime D: mixed (reattachment + coshedding) flow.

wake for both higher and lower Re is characterized by Kármán vortex streets. The similarity between the two flow conditions has been confirmed for three side-by-side prisms [27]. It is expected that the results at the current Re are useful to understand the flow physics over a large range of Re.

2.2. Computational domain and mesh

Fig. 1(a) demonstrates the schematic of the computational domain. Nine square prisms are placed in a 3×3 arrangement with the free-stream direction parallel to the prism rows. A Cartesian coordinate system is employed, and the direction of the x-axis is the same as the freestream direction, and the direction of y-axis is perpendicular to the freestream. The flow inlet and outlet are set to be $L_u = 45D$ and $L_d = 90D$, respectively (Fig. 1a). The $H = 85D$ is the height of the computational domain. At the inlet, a uniform velocity profile is imposed. Symmetric boundaries are employed on the upper and lower lateral boundaries. No-slip conditions are applied to all surfaces of the prisms. The surfaces of the centre prism (prism 5) are heated and maintained at $T^* = 1$. All other prisms have adiabatic surfaces, no heat transfer through the walls. The freestream flow enters the computational domain at $T^* = 0$ and will therefore carry heat away from prism 5. We set $Re = 150$ and $Pr = 7$.

Fig. 1(b) shows the grid distribution of a typical mesh in the vicinity of the prism. A structured grid system is used, with finer grids around the prism. A grid independence study is carried out, in which the time-averaged drag coefficient $\bar{C}_D$, fluctuating drag coefficient C'_D, fluctuating lift coefficient C'_L, and St are computed and compared for different grid numbers. Relevant results are listed in Table 2. As the grid number increases from $N = 121,000$ to $200,000$ and the corresponding dimensionless time-step reduces from $\Delta t^* = 0.0779$ to 0.0390, the relative variations of the above parameters are within 1%. It can thus be said that the mesh and time-step independence is achieved at $N = 121,000$ and $\Delta t^* = 0.0779$. For this grid system, the number of nodes on each side of the prism is 90 and the distance between the first grid and surface is $0.00333D$.

2.3. Validation

The validity of the numerical model is further tested by conducting simulations of the flow and heat transfer around a single prism. The predicted $\bar{C}_D$, C'_D, C'_L, and St are listed in Table 3 and compared with the literature data. The deviations of $\bar{C}_D$, C'_L, and St between the present and literature results are found to be less than 1%, 2%, and 2%, respectively, indicating that the current model can accurately predict fluid forces and vortex shedding frequency. Table 4 lists the Nusselt numbers for
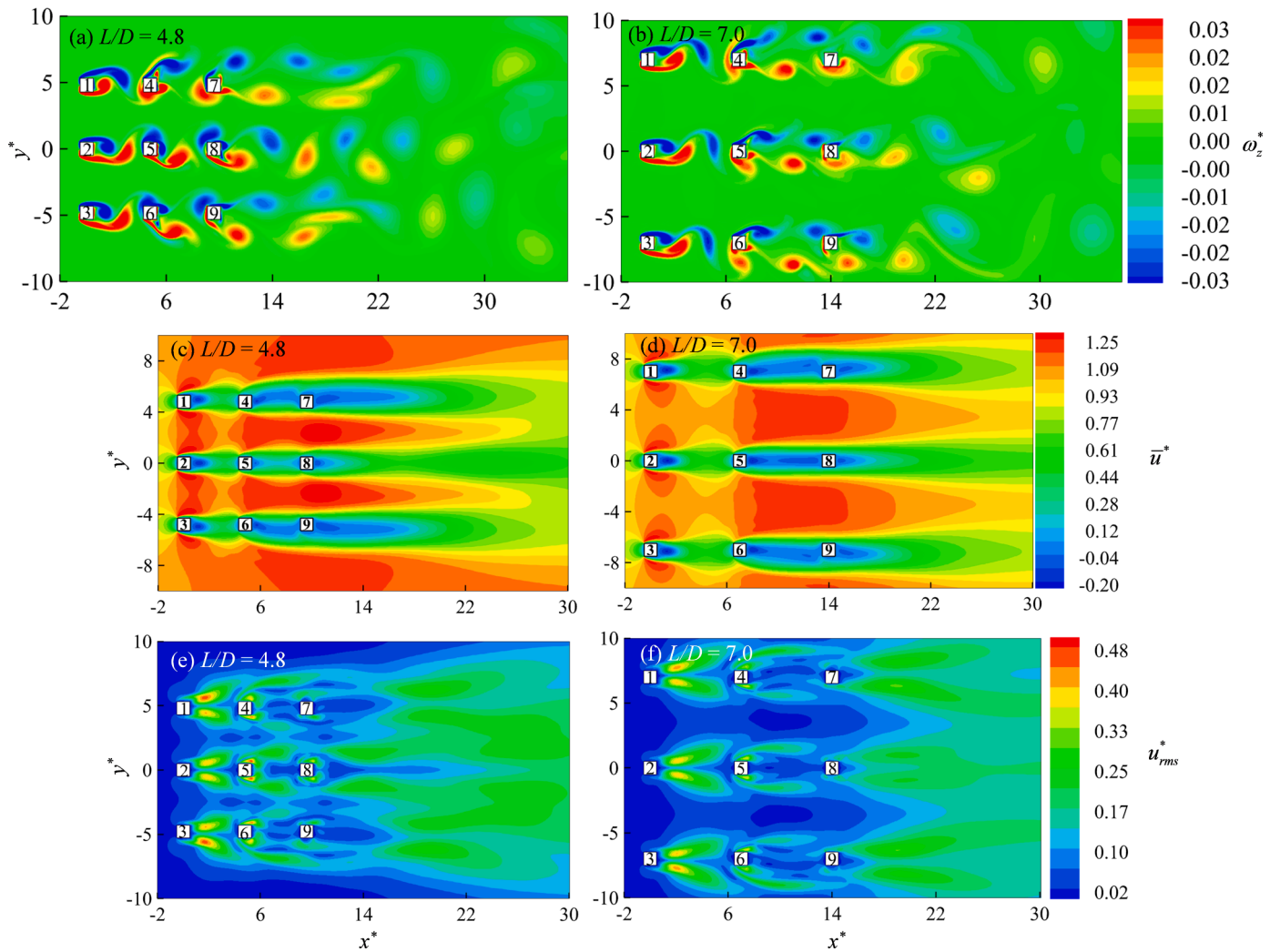
Fig. 7. (a, b) Contours of instantaneous vorticity, showing coshedding flows for all three rows of prisms. (c, d) Contour of time–averaged streamwise velocity $\overline{u}^*$. Similar recirculation bubbles form for all three rows of prisms, indicating insignificant lateral interaction between the gap flows. (e, f) Contours of fluctuating velocity u^*_{rms}, showing the vortex shedding from the upstream prisms are the strongest. (a, c, e) $L/D = 4.8$; (b, d, f) $L/D = 7.0$. Regime E: free coshedding flow.

different surfaces (Nu_{front}, Nu_{side}, Nu_{rear}) and the whole prism (Nu). In addition, the present results are compared with the corresponding results in the literature in the same table. It is found that the predicted Nusselt numbers agree well with the literature values, the maximum deviation being less than 1% although the difference in the results for the rear surface is relatively large, about 5%. For more detailed validation, kindly refer to Zafar and Alam [62], Alam et al. [63], and Abdelhamid et al. [64].

3. Flow pattern and classification

We examined the flow structures, forces, Strouhal number, and Nusselt number for $L/D = 1.2 – 7.0$ and identified five distinct flow regimes: single bluff body flow (Regime A, $L/D < 1.6$), reattachment flow (Regime B, $1.6 < L/D < 3.3$), lateral-interaction-induced coshedding flow (Regime C, $3.3 < L/D < 4.1$), mixed (coshedding + reattachment) flow (Regime D, $4.1 < L/D < 4.6$) and free coshedding flow (Regime E, $4.6 < L/D < 7.0$). The corresponding L/D range of each flow regime is illustrated in Fig. 2. The unique features of each flow regime are detailed below by selecting two L/D values close to the boundaries of each flow regime.

3.1. Regime A: single bluff body flow (L/D < 1.6)

Fig. 3(a,b) shows instantaneous vorticity contours at $L/D = 1.2$ and 1.5 spanning the investigated lower and upper boundaries of the single bluff body regime, respectively. The vorticity contours explicitly provide the strength and location of vortices, which are frequently used in the literature [68]. As the spacing between the prisms is small, all nine prisms act as a single square block or combined prism, and the vortex shedding occurs alternately from the upper and lower sides (freestream sides) of the block. The wake is characterized by a single vortex street. The flow thus features a single bluff body scenario. The flows through the streamwise gaps between the three rows of prisms are negligible at $L/D = 1.2$, not sufficiently pronounced to impact on the vortex shedding from the freestream sides of the block (Fig. 3(a)). The shear layers roll close to the base of the block. On the other hand, at $L/D = 1.5$, the gap flows are now strong enough to provide base-bleed flow (Fig. 3b), which postpones the shear layer rolling and weakens the strength of shed vortices, compared to the case of $L/D = 1.2$.

It is worth investigating the wake features in a time-mean sense [69]. Fig. 3(c,d) shows time-averaged streamwise velocity $\overline{u}^*$ contours at $L/D = 1.2$ and 1.5. Similarly, the contours of u^*_{rms} are presented in Fig. 3(e,f). While the wake region enclosed by $\overline{u}^* = 0$ is known as wake recirculation bubble, the maximum u^*_{rms} positions represent the locations of the shear
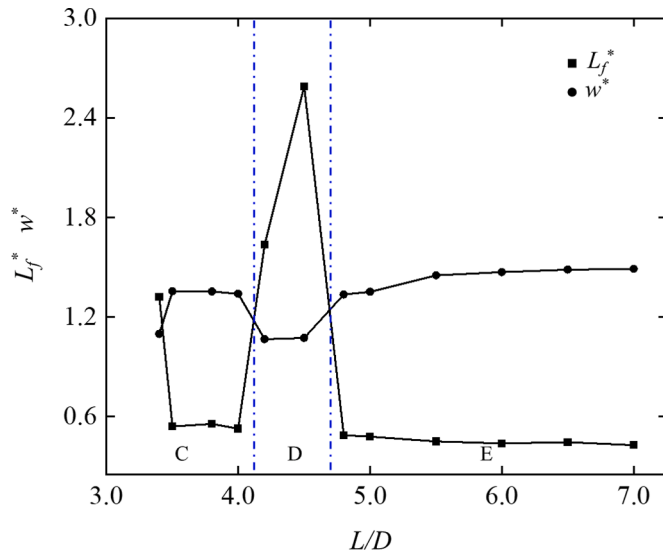
Fig. 8. Dependence on L/D of vortex formation length L_f^* and wake width w^* for prism 5. The L_f^* and w^* are inversely correlated. Regime D has a higher L_f^* than Regimes C and E since the reattachment flow upstream tends to weaken the vortex shedding of prism 5. The dash-doted lines indicate the boundaries between different flow regimes.

layer rolling [20,70–72]. The $\bar{u}^*$ in the streamwise gaps of the prisms is nearly zero at $L/D = 1.2$ (Fig. 3(c)) but noticeable at $L/D = 1.5$ (Fig. 3 (d)), diminishing along the gaps before rapid reductions at the final exits of the gaps (Fig. 3(d)). The gap flows at $L/D = 1.5$, acting base bleeds, budge the shear layer rolling away from the base and make wake recirculation bubble bigger (Fig. 3(d, f)).

The vortex formation length $L_f^* (= L_f/D)$ and wake width $w^* (= w/D)$ are often used to describe the characteristics of a wake [20]. The former is defined as the streamwise distance of maximum u_{rms}^* from the center of the block, and the latter is defined as the transverse distance between the two maxima of u_{rms}^*, as marked in Fig. 3(e,f). With L/D increasing from 1.2 to 1.5, L_f^* increases from 3.673 to 11.163 whilst w^* reduces from 4.418 to 3.522. A large w^* corresponds to a large curvature of the shear layer, which could result in a small base pressure, low St and large $\overline{C}_D$ [73]. On the other hand, a large L_f^* complements weak vortex shedding, reduced the shear layer curvature, and small $\overline{C}_D$.

3.2. Regime B: reattachment flow (1.6 < L/D < 3.3)

At $1.6 < L/D < 3.3$, the gap flows are strong enough to shed vortices, thickening with increasing L/D from 2.0 (Fig. 4(a)) to 3.2 (Fig. 4(b)). Vortex shedding occurs from the three rows of the prisms, with the freestream-side shear layers separating the upstream prism and gap-side shear layers from the downstream prism. Three vortex streets thus form, featuring in the first few spatial wavelengths of vortices and then evolving into a single vortex street downstream. The vortex shedding pattern becomes chaotic because of strong interaction between the three streets which leads to the transmutation of three streets into a single street. These results are found to be comparable to those in Sewatkar et al. [24] where the chaotic flow occurred at $2 < L/D < 3$ and $Re = 140$.

The $\bar{u}^*$ fields shown in Fig. 4(c,d) reveal that $\bar{u}^*$ in the streamwise gaps is comparable to that in the freestream sides. The $\bar{u}^*$ firstly increases in the gaps of the first-column prisms because the flow passage undergoes sudden contraction. On the other hand, $\bar{u}^*$ reduces in the streamwise gaps of the second- and third-column prisms, followed by greater reductions after the exits of third-column prisms where the gap flows have a room to suddenly expand. Given the lateral distance between the freestream-side shear layers, the expansion ratio is large at $L/$ $D = 2.0$ but small at $L/D = 3.2$, as is the reduction in $\bar{u}^*$ behind the exits. They play a role in the survival of the gap vortices. As such, the metamorphosis of the three streets into a single street is faster for $L/D = 2.0$ and slower for $L/D = 3.2$. The formations of three small recirculation bubbles behind the three downstream prisms (third-column prisms) confirm the generations of three vortex streets following the three rows of the prisms.

Now multiple u_{rms}^* peaks appear in the wake, following vortex shedding from the prisms in the third column (Fig. 4(e,f)). The u_{rms}^* peaks appear weaker and closer to the prism bases for the middle row than for the outer rows. The peaks laterally spread more at $L/D = 3.2$ than at $L/D = 2.0$. Compared to Regime A, the most noticeable feature of Regime B is the importance of the two gap flows that create three distinct streets behind the block.

3.3. Regime C: lateral-interaction-induced coshedding flow (3.3 < L/D < 4.1)

Fig. 5(a, b) shows typical vorticity contours for $L/D = 3.5$ and 4.0. Compared to Regime B, the most significant difference is the appearance of vortex shedding from each of all the nine prisms. The vortices from the first- and second-column prisms impinge on the front surfaces of the second- and third-column prisms, respectively. Because of the impingements, the vortex shedding from the second-column prisms expands laterally, compared to that from the first-column prisms. As such, the third-column prisms have further laterally expanded vortex shedding, particularly from the freestream sides of the outer prisms. Zheng and Alam [40] for a row of three prisms investigated the vortex impingement process and found that a vortex from the upstream prism first bumps and then impinges on the middle prism. The bump induces a vortex on the side surface of the middle prism. On the other hand, the impingement causes an additional vortex on the front surface. The impinging, bump-induced, and impingement-induced vortices all having the same sign of rotation evolve into a triplet vortex predominantly dictated by the impinging vortex. As such, the combined vortex moves away from the wake centerline during its downstream convection.

For a single row of three prisms, Zheng and Alam [40] at the same Re $(= 150)$ found that the coshedding flow occurs only for $L/D > 4.3$. Interestingly, the coshedding flow occurs at small L/D $(= 3.3 – 4.1)$ when three rows of prisms are placed in side-by-side. What is the intrinsic reason behind it? In another investigation by Zheng and Alam [27] for a column of three prisms at the same Re, it was found that the gap flows play a role in the wake when $L/D > 1.4$, consistent with presently obtained case $L/D=1.6$, albeit a slightly large L/D because of two additional columns of the prisms.

Zheng et al. [28] for a column of three prisms, again at the same Re, observed that the middle and outer prisms together have the smallest vortex formation length at $L/D = 3.0$, followed by increasing vortex formation length up to $L/D = 7.25$. On the other hand, for a row of three prisms $(Re = 150)$, Zheng and Alam [40] found that alternating reattachment of flow occurs at $3 < L/D < 4.3$. Once the three rows of prisms are placed side-by-side, the vortex formation length shrinks in this L/D range, which results in the metamorphosis of the alternating reattachment flow into the coshedding flow. This explains why the coshedding flow materializes at $L/D = 3.3 – 4.1$ presently. In other words, in this flow regime, the lateral interactions between the three rows of prisms shorten the streamwise distance of rolling of shear layers from the prisms in each column. We, therefore, term this flow as lateral-interaction-induced coshedding flow.

Accordingly, each prism undergoes a recirculation bubble behind it (Fig. 5(c,d)), which confirms the vortex shedding from each prism. The lateral interaction is understood from the difference in flow fields between the wakes of the middle- and outer-row prisms. Fig. 5(e,f) shows typical contours of u_{rms}^* at $L/D = 3.5$ and 4.0. The local maxima of u_{rms}^* are seen behind each prism, resembling those of a single prism. The u_{rms}^*
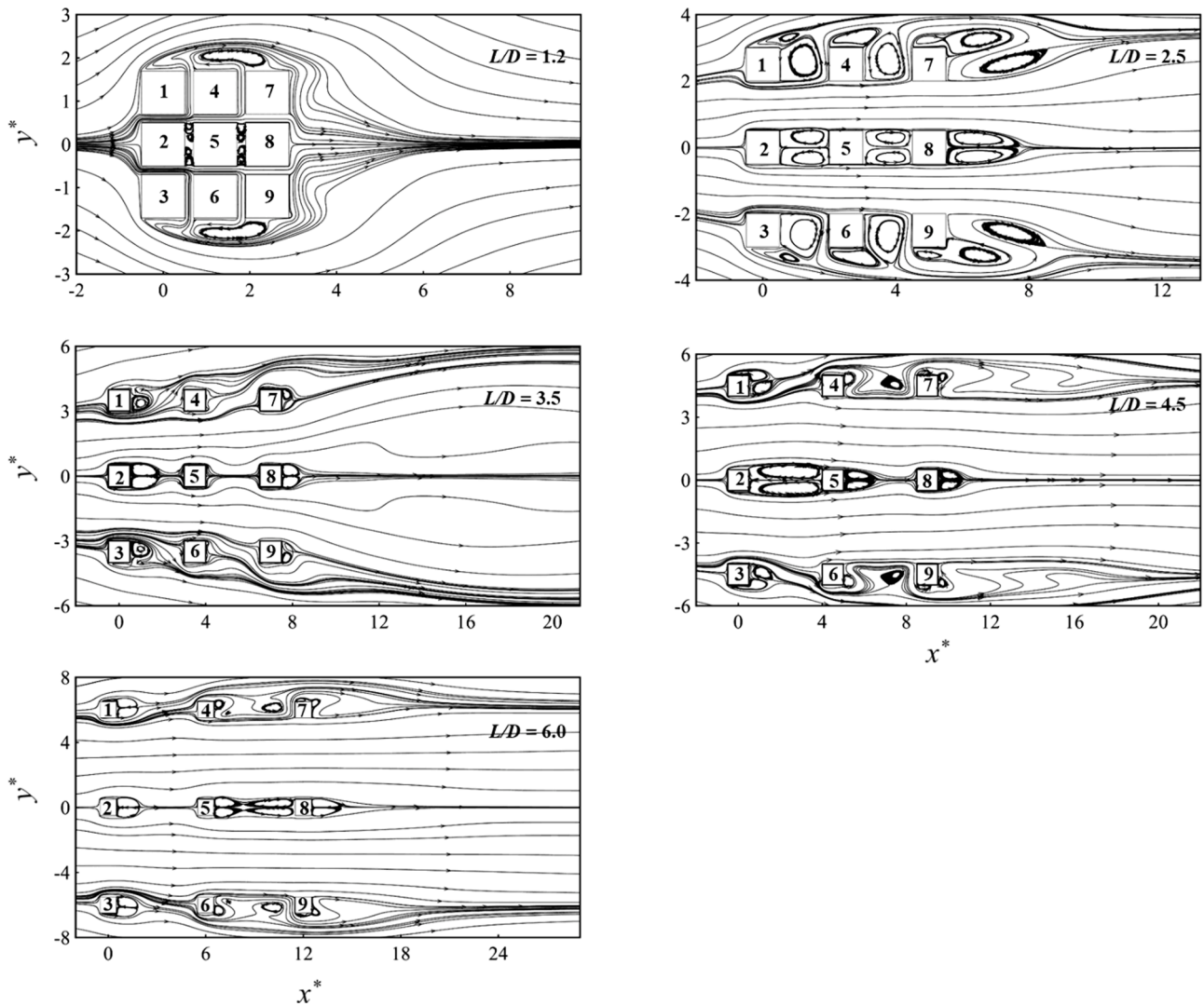
Fig. 9. Time-averaged streamline patterns of the flow field at (a) $L/D = 1.2$, (b) 2.5, (c) 3.5, (d) 4.5, and (e) 6.0, representing typical flow patterns for Regimes A-E, respectively. Regions enclosed by streamlines represent recirculation bubbles, which are normally linked to inefficient heat transfer. There is no well-organized recirculation bubble around prism 5 at $L/D = 3.5$, indicating enhanced heat transfer at Regime C.
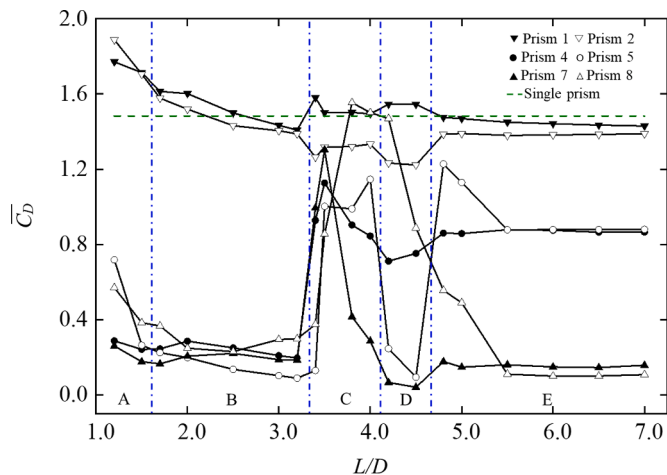

Fig. 10. Variations with L/D of time-averaged drag coefficients of different prisms. Vertical dashed-dotted lines are the boundaries of different flow regimes. The horizontal dashed line represents the data for a standalone (single) prism. The most dramatic variations occur as the flow evolves from reattachment flow B to lateral-interaction-induced coshedding flow C.

peaks are robust for the second-column prisms at $L/D = 3.5$ as are those for prisms 5 and 8 at $L/D = 4.0$. The lateral interactions and coupling of the vortices from the middle-row prisms with those from outer-row prisms make u_{rms}^* peaks strong for prisms 5 and 8 (Fig. 5(b)).

3.4. Regime D: mixed (coshedding + reattachment) flow (4.1 < L/D < 4.6)

The flow pattern in this regime includes a combination of coshedding and reattachment flows for the outer- and middle-row prisms, respectively (Fig. 6(a,b)). The vortex shedding occurs from each prism in the upper and lower rows while the shear layers of the upstream prism in the middle row reattach on the following prism. The second and third prisms in the middle row, however, have coshedding flow. At $L/D = 4.2$, the shear layer reattachment occurs on the leading corner of the middle prism (Fig. 6(a)). On the other hand, the reattachment occurs on the side surface for $L/D = 4.5$ (Fig. 6(b)). That is, the reattachment position postpones with increasing L/D from 4.2 to 4.5. This may be contradictory to our intuition for a row of two prisms or cylinders that an increase in L/D would cause a shift in the reattachment position upstream [1,31, 74]. Recall that this mixed flow pattern (4.1 < L/D < 4.6) follows the lateral-interaction-induced coshedding flow pattern ($L/D = 3.3 - 4.1$)
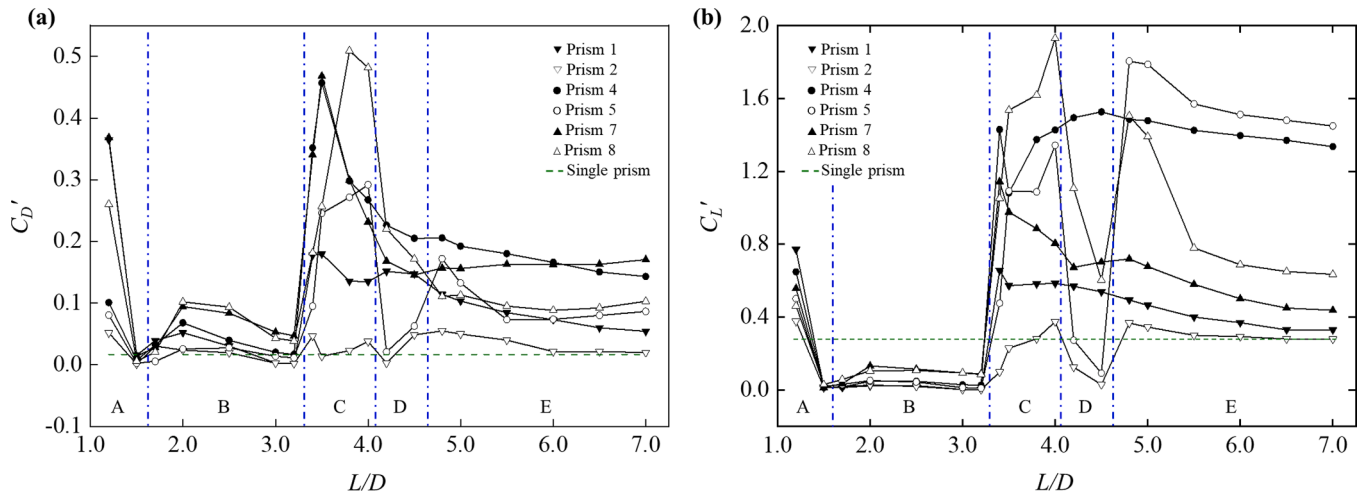
Fig. 11. Dependences on *L/D* of (a) fluctuating drag and (b) fluctuating lift coefficients. Vertical dashed-dotted lines are the boundaries of different flow regimes. The horizontal dashed line represents the data for a standalone (single) prism. The fluctuating drag coefficient of each prism is generally higher than a standalone prism and peaked in Regime C, which is characterized by the lateral interaction between different rows of prisms. Prisms 4 and 5 in Regimes C-E have significantly higher fluctuating lift and drag coefficients than the standalone prism.
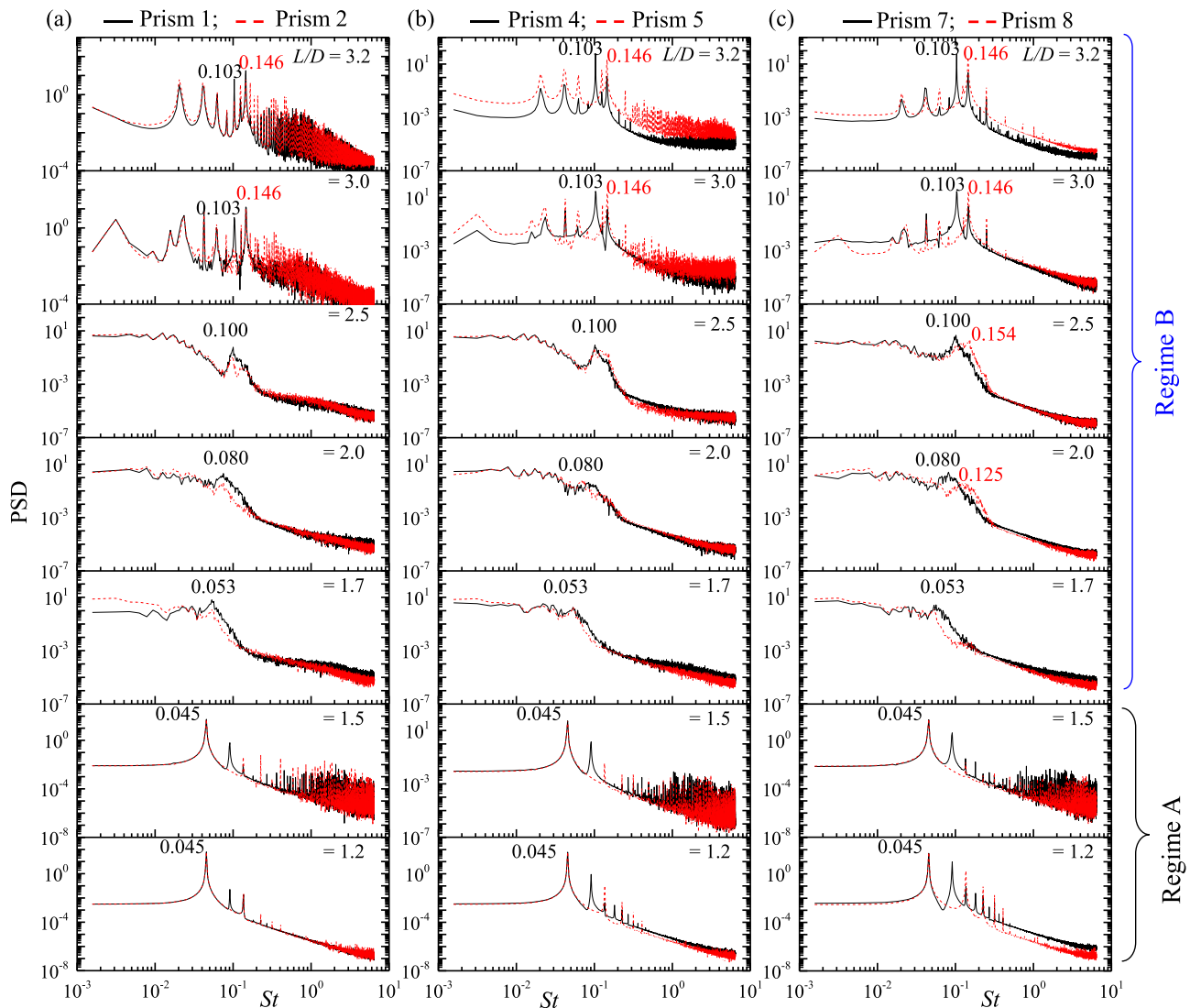

Fig. 12. Power spectra of fluctuating lift of (a) prisms 1 and 2; (b) prisms 4 and 5; and (c) prisms 7 and 8 at *L/D*=1.2 - 3.2 (Regimes A and B). In Regime A, all prisms have the same predominant Strouhal number. In Regime B, the peaks are broadbanded.
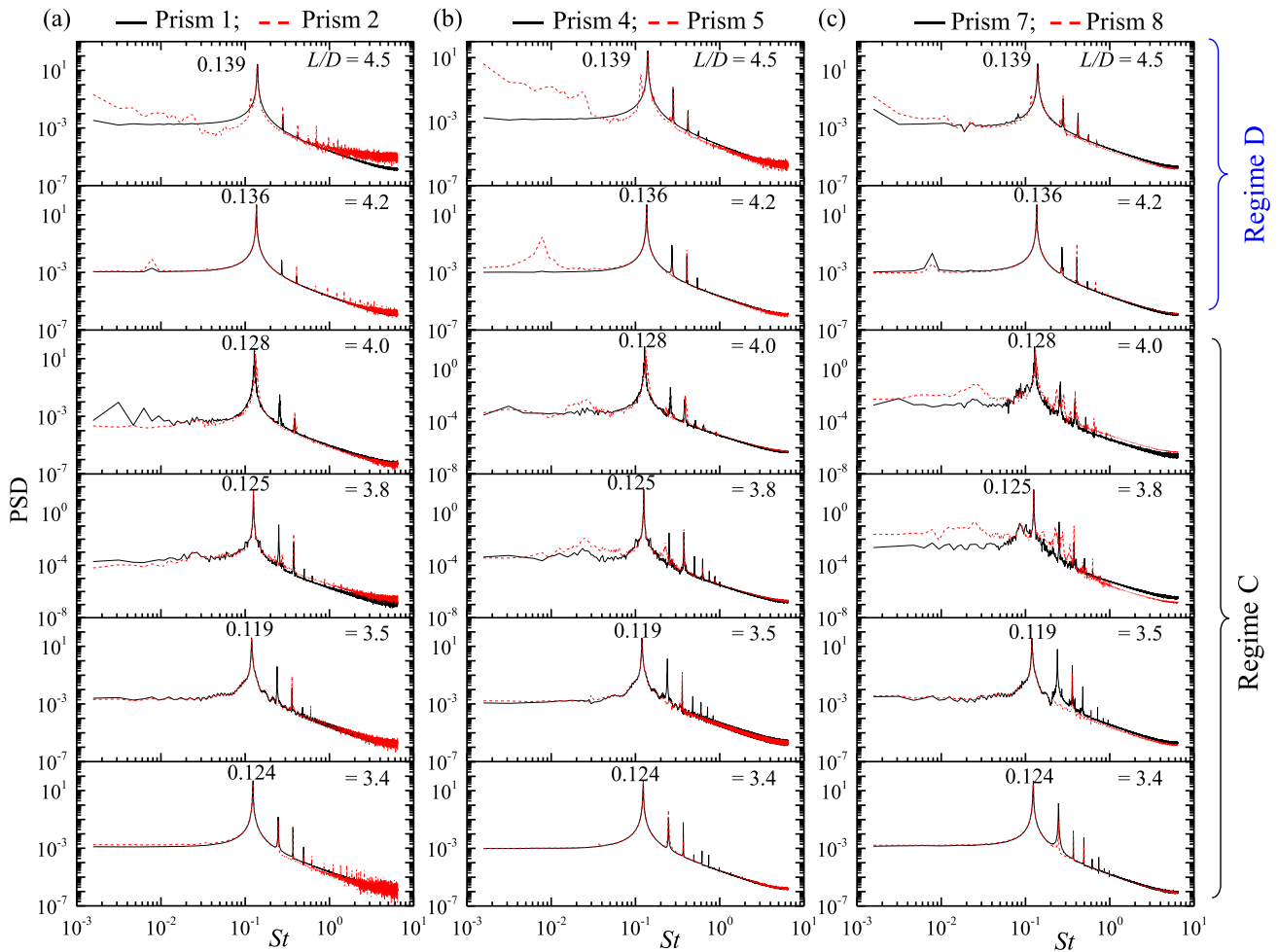
Fig. 13. Power spectra of fluctuating lift of (a) prisms 1 and 2; (b) prisms 4 and 5; and (c) prisms 7 and 8 at $L/D = 3.4 - 4.5$ (Regimes C and D). In Regime C, the power spectrum peaks are sharp and strong. In Regime D, the power spectra differ between the outer- and middle-row prisms because of the mixed flow feature of this regime.

where the lateral interaction reduces the vortex formation length.

As the lateral interaction weakens with increasing L/D, the vortex formation length elongates, which makes it possible to postpone the position of the shear layer reattachment.

The occurrence of the reattachment and coshedding flows is also further confirmed from $\overline{u}^*$ fields (Fig. 6(c,d)). As seen in the figure, the recirculation bubble in the gap between prisms 2 and 5 is strong, large, extended up to the front surface of prism 5, which is starkly different from that in the other gaps. The extended recirculation bubble in the gap between prisms 2 and 5 substantiates the reattachment flow. The lateral interactions between the three rows of prisms are still considerable as the $\overline{u}^*$ field in the two streamwise gaps is different from that in the freestream sides. The lateral interactions dwindle as L/D increases from 4.2 to 4.5.

Fig. 6(e,f) presents the contours of u_{rms}^* at $L/D = 4.2$ and 4.5. A pair of u_{rms}^* peaks appear in the gap between prisms 5 and 8, suggesting coshedding flow. At $L/D = 4.2$, the local maxima of u_{rms}^* become more apparent behind prisms 1, 3, and 8. There is no u_{rms}^* peaks behind prism 2, echoing no vortex shedding in the gap between prisms 2 and 5, but the occurrence of reattachment flow.

3.5. Regime E: free coshedding flow (4.6 < L/D < 7.0)

Fig. 7(a,b) shows instantaneous spanwise vorticity fields for $L/D = 4.8$ and 7.0. As seen in the figure, the lateral interactions between the

three rows of prisms are not enough to generate reattachment flow anymore. All three rows of prisms thus have coshedding flows. The recirculation bubbles behind the three prisms of a column are similar to each other, explaining that the lateral interactions between the prism rows are insignificant, which engenders free coshedding flow.

The u_{rms}^* fields also prove that the vortex shedding from different rows has similar strength (Fig. 7(e,f)). The peaks are strong behind the first-column prisms, gradually fainting for the second- and third-column prisms, respectively.

4. Wake characteristics

The fluid force on and heat transfer from bluff bodies are strongly connected to the flow or wake characteristics, such as recirculation, vortex shedding, formation length, and separation [8,63,64]. Since our focus is on the heat transfer from the center prism (prism 5), in this section we will pay attention to the dependence of L/D on recirculation bubbles and important wake dimensions of prism 5 to explicitly reveal the mechanism of heat transfer and forces at different L/D values.

4.1. Wake size of prism 5

Fig. 8 displays the effect of L/D on L_f^* and w^* for prism 5. Note that L_f^* and w^* are meaningful for a prism where vortex shedding from the concerned prism happens. As such, the concerning flow regimes (C, D and E) are marked in the figure. There are no data for Regimes A and B as
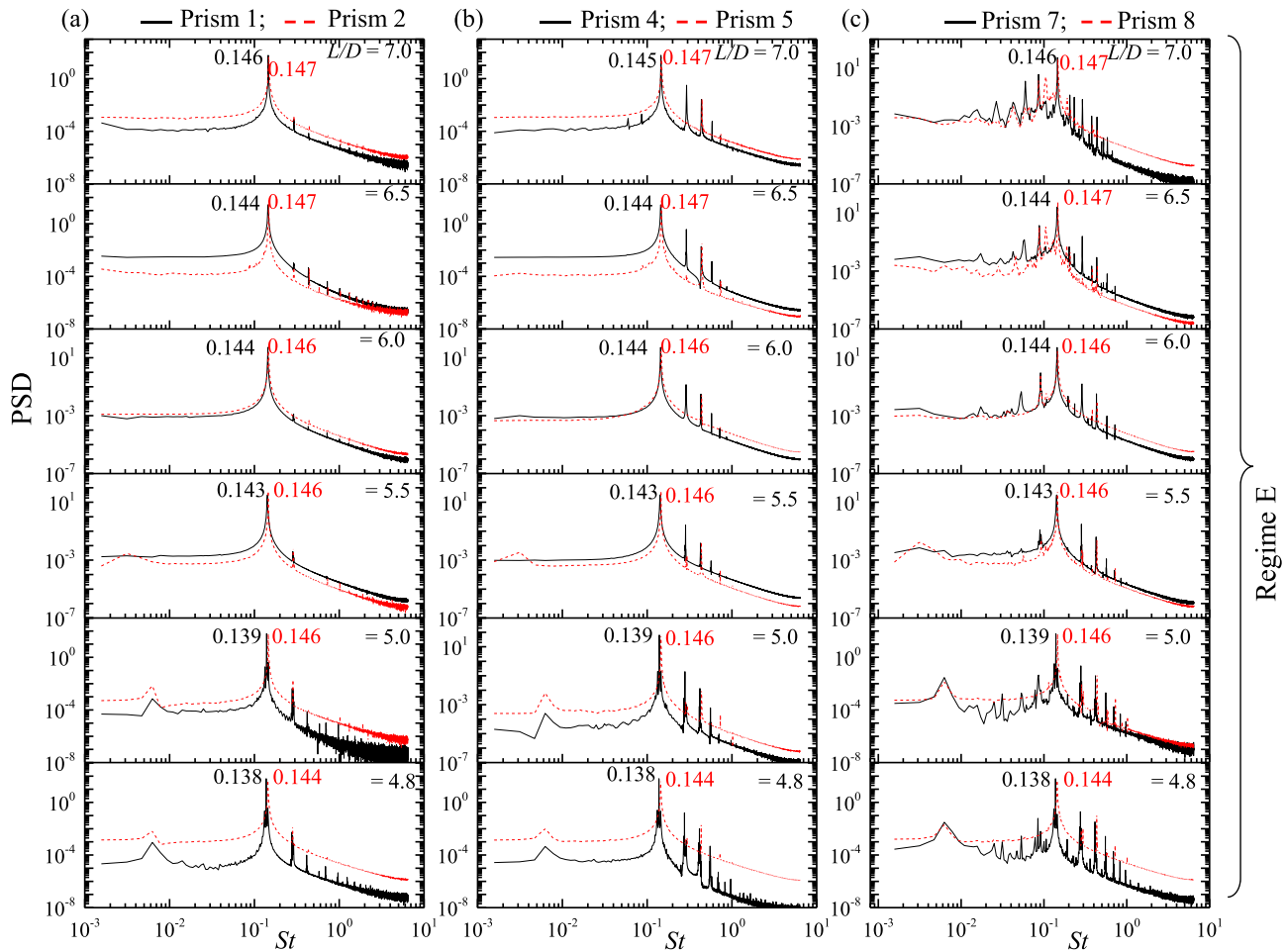
Fig. 14. Power spectra of fluctuating lift of (a) prisms 1 and 2; (b) prisms 4 and 5; and (c) prisms 7 and 8 at $L/D = 4.8 – 7.0$ (Regime E). The middle-row prisms have a higher Strouhal number than the outer-row prisms, which is attributed to a higher flow velocity around the inner prisms than the outer ones.
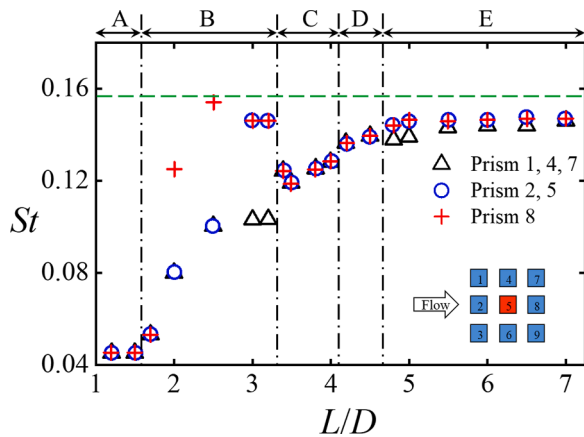

Fig. 15. Dependence of Strouhal number St on L/D. The horizontal dashed line represents the St of the standalone prism. The vertical dash-dotted lines represent the boundaries of different flow regimes. In Regime A, St is significantly lower than that of a standalone prism because of a large effective bluff width of the combined prisms. In Regime B, St differs between the prisms. In Regimes C-D, St values of the different prisms are again the same. In regime E, prisms 2, 5 and 8 have a slightly higher St than prisms 1, 4, and 7 while both are still lower than the standalone prim case.

there is no vortex shedding from prism 5 for these two flow regimes (Figs. 2a,b, 3a,b). The dependence of L_f^* and w^* on L/D essentially distinguishes the flow regimes C, D and E. The L_f^* jumps between Regimes C and D while plunging between Regimes D and E. That is, the mixed flow corresponds to a longer vortex formation length, and the two coshedding flow regimes (C and E) have comparable L_f^*. The dependence of w^* on L/D is opposite to that of L_f^*, dropping between Regimes C and D, followed by a jump between Regimes D and E. In Regime E, the w^* grows with increasing L/D while L_f^* declines. In other words, w^* and L_f^* are inversely connected. For a single prism, Bai and Alam [75] identified a similar inverse relationship between w^* and L_f^* for a large range of Re.

4.2. Recirculation bubbles

Fig. 9 shows time-averaged streamline patterns of the flow field for Regimes A-E. Regions enclosed by streamlines represent recirculation bubbles. There are two types of recirculation bubbles: one is the wake recirculation bubble that forms at the base of a prism, and the other is the separation bubble that forms on the side surfaces of the prism. The latter is the recirculation induced by the flow separation. Recirculation bubbles are normally linked to inefficient heat transfer as they are characterized by a small magnitude of flow velocity. The visualization of recirculation bubbles would thus provide useful information on the heat transfer characteristics of the flow. At $L/D = 1.2$ (Regime A), a pair of large recirculation bubbles form on the upper and lower surfaces of the block, with multiple small bubbles trapped in the gaps between prisms 2, 5 and 8 (Fig. 9(a)). Both the number of recirculation bubbles and the
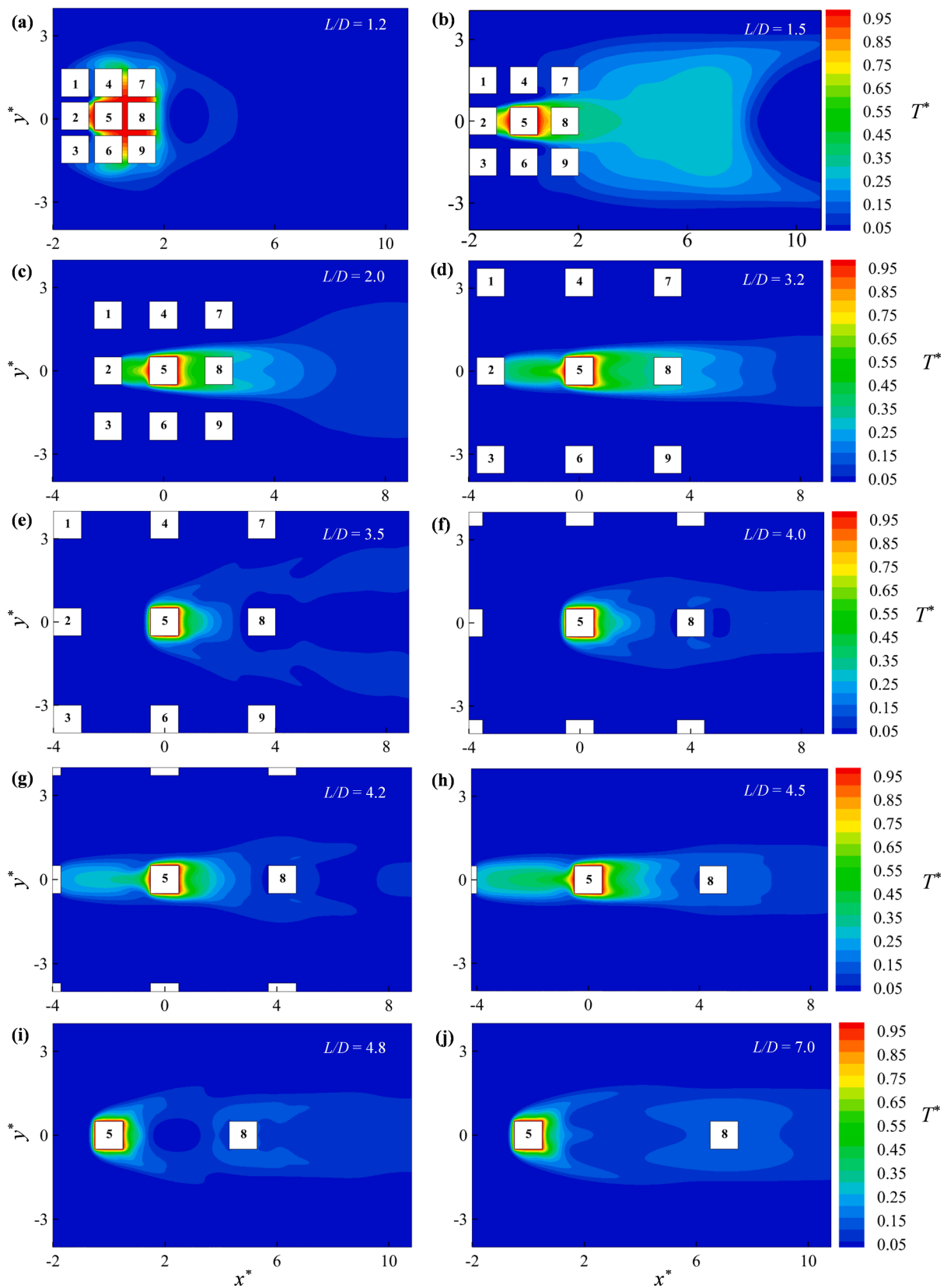
Fig. 16. Time-averaged normalized temperature distributions with constant wall temperature of Prism 5. (a) $L/D = 1.2$, (b) 1.5, (c) 2.0, (d) 3.2, (e) 3.5, (f) 4.0, (g) 4.2, (h) 4.5, (i) 4.8, and (j) 7.0. In Regime A ($L/D = 1.2$ and 1.5), the insignificant flow through the gaps causes a large high-temperature region around prism 5. In Regime B ($L/D = 2.0$ and 3.2), the temperature reduces in the two gaps as well as around prism 5 because of the enhanced flow through the gaps. In Regime C ($L/D = 3.5$ and 4.0), the coshedding flow improves fluid mixing, hence reducing the area of the high-temperature region around prism 5. In Regime D ($L/D = 4.2$ and 4.5), the temperature in the gap between prisms 2 and 5 increases because of the reattachment flow appearing for prisms 2 and 5. Temperature distribution in Regime E ($L/D = 4.8$ and 7.0) is similar to Regime C because of the similar coshedding flow features.
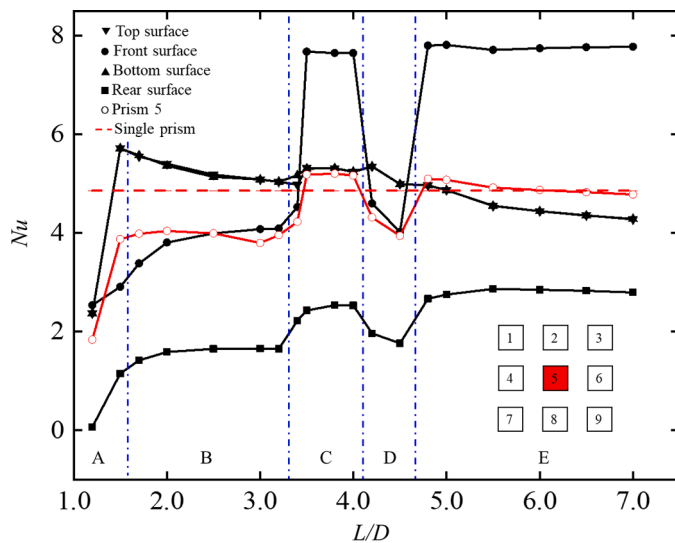
Fig. 17. Effect of *L/D* on time-averaged Nusselt number *Nu* of prism 5 and of its different surfaces. The overall *Nu* in regime C is about 10% higher than that of the standalone prism, indicating that the interaction of flow structures between different prisms could enhance the heat transfer. The *Nu* of all surfaces is influenced by the gap flow effect and increases as the flow evolves from Regimes A to B. The *Nu* of front and rear surfaces is enhanced by the appearance of coshedding flows and dips in Regime D, where the mixed flow appears.

complexity of the flow structure increase when *L/D* is increased to 2.5 (Fig. 9(b)). Now each gap of the outer-row prisms has one wake recirculation bubble, and each gap of the middle-row prisms has a pair of counter-rotating wake bubbles that are strictly confined in the gaps. Each freestream side surface of the outer-row prisms undergoes a recirculation bubble due to the flow separation. As *L/D* increases to 3.5 (Regime C), there are no well-organized wake recirculation bubbles for the upper- and lower-row prisms but are for prisms 2 and 8 in the middle row. Unlike that for *L/D* = 2.5, the wake recirculation bubble behind prism 2 does not extend up to prism 5. This could lead to an improved heat transfer from prism 5 for *L/D* = 3.5, which will be shown later. In addition, there is no wake recirculation behind prism 5, which may further enhance the heat transfer. The streamline pattern around prism 5 resembles a creeping flow. At *L/D* = 4.5 (Regime D), again the gap before prism 5 has a pair of recirculation bubbles extending up to its front surface. The rear surface of the prism also experiences two small wake recirculation bubbles. The presence of bubbles on the front and rear surfaces may hinder the heat transfer from prism 5. The front-surface recirculation bubbles for prism 5 vanish at *L/D* = 6.0 while the rear-surface bubbles remain, which may enhance heat transfer compared to the case of *L/D* = 4.5.

5. Fluid forces

Fluid forces are integral parameters, which characterize the flow structure around the prisms. Here $\overline{C}_D$, C'_D and C'_L of each prism are calculated from the simulation results and linked to different flow regimes.

5.1. Time-mean drag coefficients

Fig. 10 shows the dependence of $\overline{C}_D$ on *L/D*. As a prism in the upper row has the same time-mean forces as the corresponding prism in the lower row, results are presented for the upper- and middle-row prisms only. The horizontal dashed line represents the $\overline{C}_D$ of the standalone prism. In Regime A, the prisms in the first column (prisms 1, 2) have higher $\overline{C}_D$ values than the standalone prism. It results from low pressure generated in the gap between first- and second-column prisms. This

effect tends to weaken in Regime B. In Regimes C and D where the flows along the streamwise gaps of the prisms are considerable, $\overline{C}_D$ of prism 1 is higher and that of prism 2 is lower, compared to that of the standalone prism. Prisms 1 and 2 in Regime E have comparable $\overline{C}_D$ to the standalone prism.

The $\overline{C}_D$ values of prisms 4 and 5 are completely different from the standalone scenario. Since prisms 4 and 5 are in the wakes of the first-column prisms, the pressure on their front faces is significantly smaller than the first-column prism counterpart. This results in a smaller $\overline{C}_D$ in Regimes A and B involving single-body and reattachment flows, respectively. Compared with those in other regimes, $\overline{C}_D$ values of prisms 4 and 5 are large in Regimes C and E both involving coshedding flows. Prism 4, however, undergoes a higher $\overline{C}_D$ in Regime D than prism 5 as the flow over the first-row prisms is coshedding but that over prisms 2 and 5 is reattached (Fig. 6(a,b)). In the same flow regime, prism 8 has a higher $\overline{C}_D$ than prism 5 since the flow between prisms 5 and 8 is coshedding (Fig. 6(a,b)).

It is known that, for two tandem cylinders, the downstream cylinder experiences a higher $\overline{C}_D$ in the coshedding flow regime than in the reattachment flow regime [11,31,76]. This makes the dramatic changes of $\overline{C}_D$ at the borders between Regimes C and D and between Regimes D and E. In Regime E where the prisms are apart from each other, the $\overline{C}_D$ dramatically plunges from the first-column prisms to the second-column prisms and then to the third-column prisms. The drop between the first- and second-column prisms is about 35% (*L/D* > 5.5), and that between the second- and third-column prisms is 68%. Similar observations are also made in Bao et al. [38] for six tandem prisms except for the large drop of $\overline{C}_D$ between Regimes C and D. The difference arises because of the absence of the lateral interaction of the flow for six tandem prisms in Bao et al. [38].

5.2. Fluctuating force coefficients

Fig. 11 illustrates the effect of *L/D* on C'_D and C'_L. Both C'_D and C'_L of all prisms are significantly small in Regime B, compared to the standalone prism case. They are large in Regime C where the lateral interaction between the prisms is strong. Prisms 2 and 5 have small C'_D and C'_L in Regime D as they are connected by shear layer reattachment. In general, the reattachment flow corresponds to smaller fluctuating forces than the coshedding flow [11,31]. The C'_D and C'_L thus jumps when the reattachment flow modifies to the coshedding flow and vice versa. This agrees with the occurrence of jump and drop in C'_D and C'_L at the borders between Regimes B, C and D. In Regime E, with increasing *L/D*, the C'_D and C'_L of prisms 1 and 2 approach the counterparts in the standalone prism. The C'_D is large for prisms 4 and 7 both lying in the upper row while C'_L is large for prisms 4 and 5 both nestling in the second column, compared to the prisms in other columns. The C'_L is, however, largest for prism 5 and smallest for prism 2. Global maximum C'_L and C'_D crop up for prism 8, both in Regime C.

5.3. Power spectra density functions and Strouhal number

Power spectrum analysis of lift forces was carried out to identify the vortex shedding frequencies at different flow regimes [77,78]. Fig. 12 shows the results for *L/D* = 1.2 – 3.2 covering flow Regimes A and B. In Regime A (*L/D* = 1.2 and 1.5), all prisms have similar power spectrum results, with the most significant peak at *St* = 0.045 followed by several superharmonic peaks. Interestingly, the second harmonic peak occurs for the outer-row prisms (prisms 1, 4, and 7) and the third harmonic peak for the middle-row prisms (prisms 2, 5, and 8). Other super-harmonic peaks are very small. As *L/D* is increased from 1.2 to 1.5, high-frequency noise grows at $St = 10^0$–10^1, associated with creeping flows through the streamwise gaps of the prisms (Fig. 3(d)).
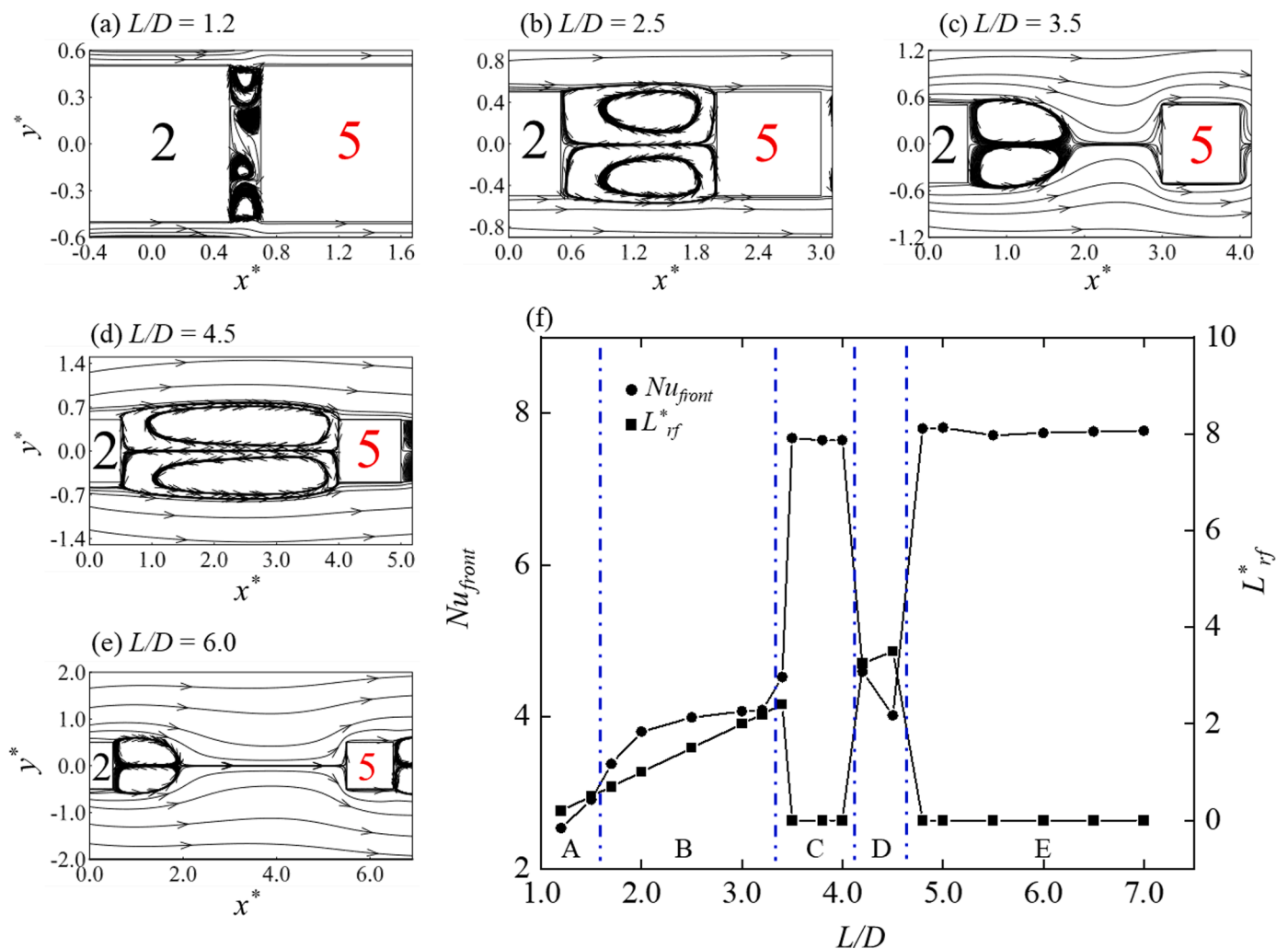
Fig. 18. Time-averaged streamlines of flow field for (a) $L/D = 1.2$, (b) 2.5, (c) 3.5, (d) 4.5, and (e) 6.0. (f) Comparison of recirculation bubble length and Nusselt number at the front surface of prism 5. There is no recirculation bubble attaching the front surface of prism 5 in Regimes C and E, which results in an enhanced heat transfer performance. The presence of a recirculation bubble reduces Nu.

At $L/D = 1.7 – 2.5$, the peaks are small, broadbanded, as expected from the nature of chaotic flow, most likely due to the formation of less-organized small-scale vortices. Particularly, prism 8 from which gap vortices are shed has the St about 1.5 times higher than the other prisms (see the power spectra at $L/D = 2$ and 2.5, third column). This 1.5-times higher St materializes for all other middle-row prisms when L/D is further increased to 3.2. The difference in shedding frequencies between the middle- and outer-row prisms results in a number of super- and subharmonic peaks in the power spectra for $L/D = 3.0$ and 3.2.

Unlike the case of chaotic flow in Regime B, all prisms have identical St in Regime C, associated with the coshedding flow (Fig. 13). Now the peaks are sharp and strong, accompanied by second- and third-harmonic peaks. Regime D has almost similar power spectral characteristics as Regime C. The similarity is ascribed to the fact that Regime D is a mixture of coshedding and reattachment flows, largely dominated by the coshedding flow, given that the reattachment flow occurs between prisms 2 and 5 only. Overall, the St generally increases with increasing L/D in both Regimes C and D, yet smaller than that ($St = 0.168$) for a standalone prism.

Fig. 14 shows power spectra for $L/D = 4.8 – 7.0$ covering Regime E. The middle-row prisms have a higher St than the outer-row prisms. The difference in St values between the two rows narrows as L/D increases from 4.8 to 7.0. For one column of four circular cylinders, Alam et al. [79] found that the two inner cylinders have a higher St than the two outer cylinders. A similar observation was shared by Zheng and Alam [27] for a column of three square prisms. The higher St for the inner prism was attributed to a higher flow velocity around the inner prism than the outer prisms. On the other hand, for three rectangular (width-to-thickness ratio $b/h = 3$) prisms aligned in a column, subjected to side wall effects, Mondal et al. [80] identified the same St for all three prisms.

Naturally, the first-column prisms have a small number of super- and sub-harmonic frequencies while the third-column prisms have more (Fig. 14). This is because vortices interact behind the third-column prisms. Similarly, the super- and sub-harmonic peaks weaken with increasing L/D since a large L/D provides less scope for the vortices to interact.

The above power spectrum results are summarized in Fig. 15, where St of each prism is plotted against L/D and compared with that of a single standalone prism. All prisms have the same St ($= 0.045$) in Regime A. This value is about 3.5 times smaller than that ($= 0.168$) of the stand-alone prism because of the effective bluff width of the three prisms to be more than three times the single prism width. In Regime B, the St is not the same for all prisms. Prism 8 has a higher St at $L/D = 2$ and 2.5 compared to the other prisms in the same row (prisms 2 and 5) and prisms in the first row (prisms 1, 4, and 7).

As L/D is increased to 3.0 and 3.2, the entire second-row prisms possess the same St, higher than the first-row prisms. Again, an identical

St is observed for all prisms in Regimes C and D, largely associated with the coshedding flow, as the reattachment flow occurring between prisms 2 and 5 only at Regime D does not contribute much to the entire flow. In Regime E, the *St* of all prisms in the second row is the same, slightly higher than that in the first row. As *L/D* increases, the difference in *St* between the first- and second-row prisms gets small because of the weakened lateral interaction between prisms.

6. Heat transfer characteristics

Heat transfer characteristics as well as the correlations between heat transfer and flow patterns are discussed in this section. Temperature fields for different flow regimes are presented while the Nusselt number for prism 5 presented illustrates the heat transfer performance of the flow at different *L/D* values.

6.1. Temperature field

As mentioned before, prism 5 is heated with constant wall temperature. It would be interesting to understand how the above five flow patterns contribute to the heat transfer from prism 5 or how the temperature field is distributed around the neighbored prisms. Fig. 16 shows the time-averaged normalized temperature *T** distributions for different *L/D* values. At *L/D* = 1.2, prisms 2, 4 and 6 – 9 endure a high *T** although only prism 5 is heated (Fig. 16a). Particularly, prism 8 undergoes extreme *T** among others. This is because of the insignificant flow through the gaps. It is seen that heat flows sideways through the lateral gap between second- and third-column prisms. The alternate vortex shedding from the outer sides of the combined block makes the pressure low on the side faces of the block, which sucks flow through the lateral gaps.

With the increase of *L/D* to 1.5 (Fig. 16b), the two streamwise-gap flows play a role in heat transfer, reducing the temperature in the streamwise gaps, although the temperatures on the front and rear surfaces of prism 5 are still high due to the weak lateral-gap flows. At *L/D* = 2.0 and 3.2 (Regime B, Fig. 16c, d), an apparent change is the reduction of temperature in the gaps between prisms 2 and 5 and between prisms 5 and 8. This is the direct result of the increased flow recirculation in the gaps. The temperature immediately behind the block also diminishes because of the reduction in the vortex formation length, compared to the case of *L/D* = 1.5. Prisms 5 and 8 are yet surrounded by hot fluid.

The temperature fields at *L/D* = 3.5 and 4.0 (Regime C, Fig. 16e, g) are distinct from those at *L/D* = 2.0 and 3.2 (Regime B). Temperature dramatically reduces in the gaps between prisms 2 and 5 and between prisms 5 and 8. Prism 8 is not surrounded by hot fluid anymore, but prism 5 is. The distinction happens because of the occurrence of vortex shedding from each prism (coshedding flow) or enhanced fluid mixing in other words. At *L/D* = 4.2 and 4.5 (Regime D, Fig. 16g, h), the temperature field bears similarity with that at Regime B except that the temperature around prism 8 in Regime D is not as high as that in Regime C. The similarity comes from the fact that shear layers in the case of Regime B are reattached for the gaps of prisms 2, 5 and 8 while those in the case of Regime D are reattached for the gap of prisms 2 and 5 and rolling for the gap of prisms 5 and 8.

Regime E (*L/D* = 4.8 and 7.0, Fig. 16i, j) has a qualitatively similar temperature field to Regime C as the characteristics of the two flow structures are similar to each other, both regimes having coshedding flow. The temperature around prism 8 is slightly smaller for Regime C than for Regime E, although interspacing between the prisms is smaller for the former regime. This implies that the lateral interaction between the prisms for Regime C enhances fluid mixing and heat transfer.

The above discussion finds some coherences between the temperature field and characteristic flow patterns, including the impacts of shear layer reattachment, flow recirculation, vortex shedding, etc. It may lead to finding a way to control and optimize the temperature field by making use of specific flow features.

6.2. Nusselt number of prism 5

The heat transfers from prism 5 and its surfaces were calculated based on Eqs. (9)–(12). Fig. 17 presents the dependence of time- and surface-averaged Nusselt number (*Nu*) on *L/D* for prism 5 and its surfaces. The *Nu* for the front and rear surfaces increases in Regimes A and B, followed by a jump at the transition between Regimes B and C. It remains more or less constant in Regime C and dips at the transition between Regimes C and D before leaping at the transition between Regimes D and E. The observation suggests that *Nu* jumps when the flow transmutes from reattachment to coshedding. On the other hand, *Nu* dips when the flow transmutation occurs oppositely, from coshedding to mixed. The *Nu* for the side (top and bottom) surfaces does not show a significant jump or dip associated with the flow transmutation but does with the absence and presence of the flow in the streamwise gaps, see the *Nu* jump between *L/D* = 1.2 and 1.5. The *Nu* of the rear surface is much smaller than that of the front and side surface, which is a common scenario for the flow around a bluff body [63,64]. The coshedding flow provides the largest *Nu* on the front surface, about 1.5 and 3 times that on the side and rear surfaces, respectively.

Contributed largely by the front surface, the overall *Nu* of prism 5 is maximum in Regimes C and E. Particularly at regime C, it is about 10% higher than that of the standalone prism. The magnitudes of *Nu* are similar in Regimes B and D that are reattachment and mixed flows, respectively, with the flow between prisms 2 and 5 being of reattachment for both regimes. This explains why the *Nu* magnitudes are similar in the two regimes. Compared with that of a single prism, the *Nu* of prism 5 is high in Regime C and low in Regimes A, B and D. That is, the interaction of flow structures between different prisms can either enhance or reduce the heat transfer performance, depending on the types of the interaction.

It is worth explaining why the *Nu* of prism 5 is high in Regime C. It is understood that the high *Nu* stems from the enhancement of heat transfer on the front and rear surfaces of the prism (Fig. 17). For this flow regime, none of these two surfaces undergoes recirculation bubbles, the flow around the prism resembling a creeping flow (see streamline pattern around prism 5 in Fig. 9c). Since the flow is attached on all surfaces of the prism, the boundary layer flow over the surfaces can extract more heat from the prism. Alam et al. [63] found that the boundary layer region on the surface largely contributes to the heat transfer while early flow separation making the boundary layer region shorter reduces the heat transfer. The above findings are useful, illuminating the possibility to promote heat transfer or avoid penalties by selecting appropriate *L/D*.

The *Nu* on the front surface is found to change most dramatically with increasing *L/D* (Fig. 17). We are thus interested in seeing flow characteristics on the front surface of prism 5. Typical streamlines of the flow field for different *L/D* values are shown in Fig. 18(a–e) to visualize the recirculation bubbles in the gap between two prisms, i.e. prisms 2 and 5. The gap is entirely occupied by the flow recirculation for *L/D* = 1.2 (Regime A), 2.0 (Regime B) and 4.5 (Regime D). On the other hand, for *L/D* = 3.5 and 6.0, the flow recirculation is absent on the front surface of prism 5 but present on the rear surface of prism 2. It is expected that the recirculation bubble forming in the gap may play a role in the heat transfer from the front surface of prism 5. Fig. 18(f) shows the relationship of the recirculation bubble size (L_{rf}^*) and *Nu* of the front surface of prism 5. Here, L_{rf}^* is the streamwise length of the recirculation bubble that appears on the front surface of prism 5. For example, for *L/D* = 2.5, the L_{rf}^* is the distance from the front surface of prism 5 to the rear surface of prism 2. On the other hand, $L_{rf}^* = 0$ when the recirculation bubble is not on the front surface but away from it, see Fig. 18(c, e).

A clear relationship between L_{rf}^* and *Nu* is observed. The L_{rf}^* linearly increases with *L/D* in Regimes A and B as the bubble essentially occupies the entire gap between prisms 2 and 5 (Fig. 18(a,b)). The *Nu* is also

found to increase with L/D, albeit non-linearly, in the same regimes. In Regimes C, the recirculation bubble is absent on the front surface of prism 5, the front surface experiencing an approaching flow instead of reverse flow. Here, L_{rf}^* is presented as zero. The same scenario prevails in Regime E. The Nu on the front surface is large in Regimes C and E. The observation suggests that to enhance heat transfer the recirculation bubble should be made either absent or bigger as much as possible.

7. Conclusions

The flow and heat transfer around nine square prisms in a 3×3 array are investigated for $L/D = 1.2 - 7.0$ at $Re = 150$. The investigation focuses on the effect of L/D on flow structure, fluid force, Strouhal number, wake size, recirculation bubbles, and Nusselt number. In addition, we shed light on how the flow structure determines heat transfer performance. As L/D is varied from 1.2 to 7.0, five flow regimes are identified, each having distinct flow features and a distinct range of L/D. They are single bluff body flow (Regime A, $L/D < 1.6$), reattachment flow (Regime B, $1.6 < L/D < 3.3$), lateral-interaction-induced coshedding flow (Regime C, $3.3 < L/D < 4.1$), mixed (reattachment + coshedding) flow (Regime D, $4.1 < L/D < 4.6$) and free coshedding flow (Regime E, $4.6 < L/D < 7.0$). Several interesting features characterize the lateral-interaction-induced coshedding flow. Firstly, the lateral interaction advances the coshedding flow to a smaller L/D. Secondly, the flow around the center prism resembles a creeping flow, no recirculation bubble forms on the front or rear surface of the prism.

The fluid forces ($\overline{C}_D$, C_D' and C_L') are small in reattachment flow regime and large in lateral-interaction-induced coshedding flow. When the flow transits from reattachment to coshedding or vice versa, the transition is accompanied by a drastic rise or drop in fluid forces. For prism 5, $\overline{C}_D$ jumps from 0.09 to 1.0 when the flow evolves from Regime B to Regime C, and then dips to less than 0.1 again as the flow transmutes from Regime C into Regime D. At a sufficiently large $L/D = 5.5$–7.0 (free coshedding flow), $\overline{C}_D$ drops by 35% from the first-column prisms to the second-column prisms and by 68% from the second-column prisms to the third-column prisms.

All prisms have the same St for the single bluff body flow, lateral-interaction-induced coshedding flow and mixed flow regimes. This is, however, not the case in the reattachment flow and free coshedding flow regimes. In the case of the free coshedding flow, the St of the prisms in the second row is higher than that in the first row. An increase in L/D weakens the lateral interaction and reduces the difference in St between the first- and second-row prisms. The vortex formation length of the center prism leaps between the lateral-interaction-induced coshedding flow and mixed flow while it dips between the mixed flow and free coshedding flow. The wake width varies oppositely to the vortex formation length.

The Nusselt number of the center prism is maximum in the lateral-interaction-induced coshedding flow regime, about 10% higher than that of a standalone prism. The maximum heat transfer results from the creeping flow generated around the center prism, which is characterized by the absence of front- and rear-surface recirculation bubbles. The heat transfer jumps when the reattachment flow modifies to the lateral-interaction-induced coshedding flow. It is found that the gap recirculation bubble plays a predominant role in the heat transfer from the front surface. Heat transfer enhances with a increasing bubble size. Further enhancement comes into being when the bubble on the front surface disappears. The coherence between heat transfer and flow patterns, including the impacts of shear layer reattachment, flow recirculation, and vortex shedding on heat transfer is demonstrated.

CRediT authorship contribution statement

Zhanying Zheng: Methodology, Investigation, Software, Writing – original draft, Funding acquisition. **Md. Mahbub Alam:** Methodology, Investigation, Resources, Writing – review & editing. **Qinmin Zheng:** Conceptualization, Software, Writing – review & editing. **S. Dhina-karan:** Conceptualization, Methodology, Writing – review & editing. **Md. Islam:** Conceptualization, Methodology, Writing – review & editing, Funding acquisition.

Declaration of Competing Interest

The authors declare that they have no known competing financial interests or personal relationships that could have appeared to influence the work reported in this paper.

Acknowledgments

References

[1] Alam MM. The aerodynamics of a cylinder submerged in the wake of another. J Fluids Struct 2014;51:393–400.

[2] Sohankar A, Etminan A. Forced-convection heat transfer from tandem square cylinders in cross flow at low Reynolds numbers. Int J Numer Method Fluid 2009; 60(7):733–51.

[3] Zhou Y, Yiu MW. Flow structure, momentum and heat transport in a two-tandem-cylinder wake. J Fluid Mech 2006;548:17–48.

[4] Liu MM, Lu L, Teng B, Zhao M, Tang GQ. Re-examination of laminar flow over twin circular cylinders in tandem arrangement. Fluid Dyn Res 2014;46(2):025501.

[5] Sohankar A, Khodadadi M, Rangraz E, Alam MM. Control of flow and heat transfer over two inline square cylinders. Phys Fluid 2019;31(12):123604.

[6] Sohankar A, Rangraz E, Khodadadi M, Alam MM. Fluid flow and heat transfer around single and tandem square cylinders subjected to shear flow. J Braz Soc Mech Sci Eng 2020;42(8):414.

[7] Wang L, Alam MM, Zhou Y. Two tandem cylinders of different diameters in cross-flow: effect of an upstream cylinder on wake dynamics. J Fluid Mech 2018;836: 5–42.

[8] Zafar F, Alam MM. Mixed convection heat transfer from a circular cylinder submerged in wake. Int J Mech Sci 2020;183:105733.

[9] Zhou Q, Alam MM, Cao S, Liao H, Li M. Numerical study of wake and aerodynamic forces on two tandem circular cylinders at Re = 103. Phys Fluid 2019;31(4): 045103.

[10] Alam MM, Zhou Y. Flow around two side-by-side closely spaced circular cylinders. J Fluid Struct 2007;23(5):799–805.

[11] Alam MM, Moriya M, Sakamoto H. Aerodynamic characteristics of two side-by-side circular cylinders and application of wavelet analysis on the switching phenomenon. J Fluid Struct 2003;18(3):325–46.

[12] Agrawal A, Djenidi L, Antonia RA. Investigation of flow around a pair of side-by-side square cylinders using the lattice Boltzmann method. Comput Fluid 2006;35 (10):1093–107.

[13] Alam MM, Sakamoto H. Investigation of strouhal frequencies of two staggered bluff bodies and detection of multistable flow by wavelets. J Fluid Struct 2005;20(3): 425–49.

[14] Alam MM, Sakamoto H, Zhou Y. Determination of flow configurations and fluid forces acting on two staggered circular cylinders of equal diameter in cross-flow. J Fluid Struct 2005;21(4):363–94.

[15] Hu JC, Zhou Y. Flow structure behind two staggered circular cylinders. Part 1. Downstream evolution and classification. J Fluid Mech 2008;607:51–80.

[16] Wong CW, Zhou Y, Alam MM, Zhou TM. Dependence of flow classification on the Reynolds number for a two-cylinder wake. J Fluid Struct 2014;49:485–97.

[17] Sumner D. Two circular cylinders in cross-flow: a review. J Fluid Struct 2010;26 (6):849–99.

[18] Zhou Y, Alam MM. Wake of two interacting circular cylinders: a review. Int J Heat Fluid Flow 2016;62:510–37.

[19] Derakhshandeh JF, Alam MM. A review of bluff body wakes. Ocean Eng 2019;182: 475–88.

[20] Alam MM, Zhou Y, Wang XW. The wake of two side-by-side square cylinders. J Fluid Mech 2011;669:432–71.

[21] Alam MM, Zhou Y. Intrinsic features of flow around two side-by-side square cylinders. Phys Fluid 2013;25(8):085106.

[22] KolÁŘ V, Lyn DA, Rodi W. Ensemble-averaged measurements in the turbulent near wake of two side-by-side square cylinders. J Fluid Mech 1997;346:201–37.

[23] Kumar SR, Sharma A, Agrawal A. Simulation of flow around a row of square cylinders. J Fluid Mech 2008;606:369–97.

[24] Sewatkar CM, Sharma A, Agrawal A. On the effect of Reynolds number for flow around a row of square cylinders. Phys Fluid 2009;21(8):083602.

[25] Chatterjee D, Biswas G, Amiroudine S. Numerical investigation of forced convection heat transfer in unsteady flow past a row of square cylinders. Int J Heat Fluid Flow 2009;30(6):1114–28.

[26] Chatterjee D, Biswas G, Amiroudine S. Numerical simulation of flow past row of square cylinders for various separation ratios. Comput Fluid 2010;39(1):49–59.

[27] Zheng Q, Alam MM. Intrinsic features of flow past three square prisms in side-by-side arrangement. J Fluid Mech 2017;826:996–1033.

[28] Zheng Q, Alam MM, Rehman S, Maiti DK. Forces and flow around three side-by-side square cylinders. Wind Struct 2019;29(1):1–13.

[29] Sakamoto H, Hainu H, Obata Y. Fluctuating forces acting on two square prisms in a tandem arrangement. J Wind Eng Ind Aerodyn 1987;26(1):85–103.

[30] Sakamoto H, Haniu H. Effect of free-stream turbulence on characteristics of fluctuating forces acting on two square prisms in tandem arrangement. J Fluid Eng 1988;110(2):140–6.

[31] Alam MM, Moriya M, Takai K, Sakamoto H. Suppression of fluid forces acting on two square prisms in a tandem arrangement by passive control of flow. J Fluid Struct 2002;16(8):1073–92.

[32] Liu CH, Chen JM. Observations of hysteresis in flow around two square cylinders in a tandem arrangement. J Wind Eng Ind Aerodyn 2002;90(9):1019–50.

[33] Kim MK, Kim DK, Yoon SH, Lee DH. Measurements of the flow fields around two square cylinders in a tandem arrangement. J Mech Sci Technol 2008;22(2):397.

[34] Yen SC, San KC, Chuang TH. Interactions of tandem square cylinders at low Reynolds numbers. Exp Therm Fluid Sci 2008;32(4):927–38.

[35] Sohankar A. A numerical investigation of the flow over a pair of identical square cylinders in a tandem arrangement. Int J Numer Method Fluid 2012;70(10):1244–57.

[36] Rastan MR, Alam MM. Transition of wake flows past two circular or square cylinders in tandem. Phys Fluid 2021;33(8):081705.

[37] Freidooni F, Sohankar A, Rastan MR, Shirani E. Flow field around two tandem non-identical-height square buildings via LES. Build Environ 2021;201:107985.

[38] Bao Y, Wu Q, Zhou D. Numerical investigation of flow around an inline square cylinder array with different spacing ratios. Comput Fluid 2012;55:118–31.

[39] Sewatkar CM, Patel R, Sharma A, Agrawal A. Flow around six in-line square cylinders. J Fluid Mech 2012;710:195–233.

[40] Zheng Q, Alam MM. Evolution of the wake of three inline square prisms. Phys Rev Fluid 2019;4(10):104701.

[41] Islam SU, Zhou CY, Ahmad F. Numerical simulations of cross-flow around four square cylinders in an in-line rectangular configuration. World Acad Sci Eng Technol 2009;33:824–33.

[42] Zhang W, Li WJ, Ye HH, Zhang DX. Numerical simulation of cross-flow around four square cylinders in a square configuration at low reynolds number. Appl Mech Mater 2013;423-426:1700–4.

[43] Abbasi WS, Shams Ul I, Saha SC, Gu YT, Ying ZC. Effect of Reynolds numbers on flow past four square cylinders in an in-line square configuration for different gap spacings. J Mech Sci Technol 2014;28(2):539–52.

[44] Chatterjee D, Biswas G. Dynamic behavior of flow around rows of square cylinders kept in staggered arrangement. J Wind Eng Ind Aerodyn 2015;136:1–11.

[45] Nguyen VL, Nguyen-Thoi T, Duong VD. Characteristics of the flow around four cylinders of various shapes. Ocean Eng 2021;238:109690.

[46] Chatterjee D. Mixed convection heat transfer from tandem square cylinders in a vertical channel at low reynolds numbers. Numer Heat Transf Part A Appl 2010;58(9):740–55.

[47] Chatterjee D, Mondal B. Forced convection heat transfer from tandem square cylinders for various spacing ratios. Numer Heat Transf Part A Appl 2012;61(5):381–400.

[48] Chatterjee D, Mondal B. Unsteady mixed convection heat transfer from tandem square cylinders in cross flow at low Reynolds numbers. Heat Mass Transf 2013;49(7):907–20.

[49] Huang Z, Xi G, Zhang W, Wen S. Mixed convection heat transfer from confined tandem square cylinders in a horizontal channel. Int J Heat Mass Transf 2013;66:625–31.

[50] Sisodia SS, Sarkar S, Saha SK. Fluid flow and mixed convective heat transfer around a semi-circular cylinder at incidence with a tandem downstream square cylinder in cross flow. Int J Therm Sci 2017;121:13–29.

[51] Dwivedi AR, Dhiman AK. Flow and heat transfer analysis around tandem cylinders: critical gap ratio and thermal cross-buoyancy. J Braz Soc Mech Sci Eng 2019;41(11):487.

[52] Zhang W, Chen X, Yang H, Liang H, Wei Y. Forced convection for flow across two tandem cylinders with rounded corners in a channel. Int J Heat Mass Transf 2019;130:1053–69.

[53] Sanyal A, Dhiman A. Wake interactions in a fluid flow past a pair of side-by-side square cylinders in presence of mixed convection. Phys Fluid 2017;29(10):103602.

[54] Sanyal A, Dhiman A. Effect of thermal buoyancy on a fluid flowing past a pair of side-by-side square bluff-bodies in a low-Reynolds number flow regime. Phys Fluid 2018;30(6):063603.

[55] Patel CG, Sarkar S, Saha SK. Mixed convective vertically upward flow past side-by-side square cylinders at incidence. Int J Heat Mass Transf 2018;127:927–47.

[56] Moussaoui MA, Mezrhab A, Naji H. A computation of flow and heat transfer past three heated cylinders in a vee shape by a double distribution MRT thermal lattice Boltzmann model. Int J Therm Sci 2011;50(8):1532–42.

[57] Barros GM, Lorenzini G, Isoldi LA, Rocha LAO, dos Santos ED. Influence of mixed convection laminar flows on the geometrical evaluation of a triangular arrangement of circular cylinders. Int J Heat Mass Transf 2017;114:1188–200.

[58] Teixeira FB, Lorenzini G, Errera MR, Rocha LAO, Isoldi LA, dos Santos ED. Constructal design of triangular arrangements of square bluff bodies under forced convective turbulent flows. Int J Heat Mass Transf 2018;126:521–35.

[59] Yoon DH, Yang KS, Choi CB. Flow past a square cylinder with an angle of incidence. Phys Fluid 2010;22(4):043603.

[60] Park D, Yang KS. Flow instabilities in the wake of a rounded square cylinder. J Fluid Mech 2016;793:915–32.

[61] Zheng Q, Alam MM, Zhou Y. The wake of three square prisms in side-by-side arrangement. Berlin, Heidelberg: Springer Berlin Heidelberg; 2016. p. 435–40.

[62] Zafar F, Alam MM. Flow structure around and heat transfer from cylinders modified from square to circular. Phys Fluid 2019;31(8):083604.

[63] Alam MM, Abdelhamid T, Sohankar A. Effect of cylinder corner radius and attack angle on heat transfer and flow topology. Int J Mech Sci 2020;175:105566.

[64] Abdelhamid T, Alam MM, Islam M. Heat transfer and flow around cylinder: effect of corner radius and Reynolds number. Int J Heat Mass Transf 2021;171:121105.

[65] Sharma A, Eswaran V. Heat and fluid flow across a square cylinder in the two-dimensional laminar flow regime. Numer Heat Transf Part A Appl 2004;45(3):247–69.

[66] Saha AK, Biswas G, Muralidhar K. Three-dimensional study of flow past a square cylinder at low Reynolds numbers. Int J Heat Fluid Flow 2003;24(1):54–66.

[67] Sahu AK, Chhabra RP, Eswaran V. Effects of Reynolds and Prandtl numbers on heat transfer from a square cylinder in the unsteady flow regime. Int J Heat Mass Transf 2009;52(3):839–50.

[68] Nakhchi ME, Naung SW, Rahmati M. Influence of blade vibrations on aerodynamic performance of axial compressor in gas turbine: direct numerical simulation. Energy 2022;242:122988.

[69] Naung SWin, Nakhchi ME, Rahmati M. High-fidelity CFD simulations of two wind turbines in arrays using nonlinear frequency domain solution method. Renew Energy 2021;174:984–1005.

[70] Alam MM, Zhou Y. Turbulent wake of an inclined cylinder with water running. J Fluid Mech 2007;589:261–303.

[71] Bloor MS. The transition to turbulence in the wake of a circular cylinder. J Fluid Mech 1964;19(2):290–304.

[72] Gerrard JH. The mechanics of the formation region of vortices behind bluff bodies. J Fluid Mech 1966;25(2):401–13.

[73] Nakaguchi H, Hashimoto K, Muto S. An experimental study on aerodynamic drag of rectangular cylinders. J Jpn Soc Aeronaut Eng 1968;16(168):1–5.

[74] Alam MM, Bai H, Zhou Y. The wake of two staggered square cylinders. J Fluid Mech 2016;801:475–507.

[75] Bai H, Alam MM. Dependence of square cylinder wake on Reynolds number. Phys Fluid 2018;30(1):015102.

[76] Alam MM. Lift forces induced by phase lag between the vortex sheddings from two tandem bluff bodies. J Fluid Struct 2016;65:217–37.

[77] Nakhchi ME, Rahmati M. Direct numerical simulations of flutter instabilities over a vibrating turbine blade cascade. J Fluid Struct 2021;104:103324.

[78] Naung SW, Nakhchi ME, Rahmati M. Prediction of flutter effects on transient flow structure and aeroelasticity of low-pressure turbine cascade using direct numerical simulations. Aerosp Sci Technol 2021;119:107151.

[79] Alam MM, Zheng Q, Hourigan K. The wake and thrust by four side-by-side cylinders at a low Re. J Fluids Struct 2017;70:131–44.

[80] Mondal R, Alam MM, Bhatt R. Effect of side walls on flow around prisms. Ocean Eng 2020;196:106797.